

Resolving Strain Localization of Brittle and Ductile Deformation in two- and three- dimensions using Graphical Processing Units (GPUs)

Yury Alkhimenkov^{1*,5}, Lyudmila Khakimova^{2,5}, Ivan Utkin^{3,4,5}, and Yury Podladchikov^{2,5}

¹Department of Civil and Environmental Engineering, Massachusetts Institute of Technology, Cambridge,
MA 02139, USA

²Institute of Earth Sciences, University of Lausanne, Lausanne, Switzerland

³Laboratory of Hydraulics, Hydrology and Glaciology (VAW), ETH Zurich, Zurich, Switzerland

⁴WSL, Birmensdorf, Switzerland

⁵Faculty of Mechanics and Mathematics, Lomonosov Moscow State University, Moscow 119991, Russia

Abstract

Shear strain localization refers to the phenomenon of accumulation of material deformation in narrow slip zones. Many materials exhibit strain localization under different spatial and temporal scales, particularly rocks, metals, soils, and concrete. In the Earth's crust, irreversible deformation can occur in brittle as well as in ductile regimes. Modeling of shear zones is essential in the geodynamic framework. Numerical modeling of strain localization remains challenging due to the non-linearity and multi-scale nature of the problem. We develop a numerical approach based on graphical processing units (GPU) to resolve the strain localization in two and three dimensions of a (visco)-hypoelastic-perfectly plastic medium. Our approach allows modeling both the compressible and incompressible visco-elasto-plastic flows. We demonstrate that using sufficiently small strain or strain rate increments, a non-symmetric strain localization pattern is resolved in two- and three-dimensions. We show that elasto-plastic and visco-plastic models yield similar strain localization patterns for material properties relevant to applications in geodynamics. We achieve fast computations using three-dimensional high-resolution models involving more than 500 million degrees of freedom. We propose a new physics-based approach explaining spontaneous stress drops in a deforming medium. We demonstrate by coupling the geomechanical model with a wave propagation solver that the rapid development of a shear zone in rocks generates seismic signal characteristics for earthquakes.

* yalkhime@mit.edu

1 Introduction

Strain localization refers to the phenomenon of strain accumulation in narrow regions which happens in rocks and in most materials, particularly metals, rocks, soils, and concrete, under different spatial and temporal scales. The physical mechanisms governing strain localization are different in different materials. Usually, localization occurs when the external load reaches a certain threshold. The strength of most geomaterials, particularly rocks, is strongly pressure-dependent, with strength increasing with increasing pressure. In the upper part of the Earth’s crust, rocks behave like brittle-elastic material. With increasing depth, growing confining pressure leads to the increase in the strength of the rocks. In the lower parts of the Earth’s crust, elevated temperatures activate the ductile regime of deformation. Plastic yielding and strain localization occurs in both brittle and ductile regimes. In this study, we will mostly explore strain localization in rocks, however, the presented methodology is applicable to model the plastic behavior of other materials with similar material properties as well. We here develop efficient numerical algorithms based on High Performance Computing (HPC) and graphical processing units (GPUs) to model strain localization in two- and three- dimensions for applications in geodynamics and earthquake physics.

Numerical modeling is an essential tool to better understand physical processes taking place on Earth (Turcotte and Schubert, 2002). During the last decades, several three-dimensional geodynamical codes have been developed to model complex physical processes: ASPECT (Kronbichler et al., 2012), Citcom (Moresi et al., 1996), DOUAR (Braun et al., 2008), FANTOM (Thieulot, 2011), Fluidity (Davies et al., 2011), I3(E)LVIS (Gerya and Yuen, 2007), MILAMIN (Dabrowski et al., 2008), pTaTin3D (May et al., 2015), PyLith (Aagaard et al., 2013) combined with PETSc (Balay et al., 2019), Rhea (Burstedde et al., 2008), Slim3D (Popov and Sobolev, 2008), TERRA (Baumgardner, 1985; Davies et al., 2013; Wilson et al., 2017), STAGYY (Tackley, 1996, 2008), Underworld2 (Moresi et al., 2007b). May and Moresi (2008) analyzed several iterative methods for inertialess flow problems arising in geodynamics. A more complex visco-elastic rheology is needed to adequately model short time-scale (Deng et al., 1998) and long time-scale processes in geodynamics (Farrington et al., 2014; Jaquet et al., 2016; Olive et al., 2016). All these codes are mainly implemented using CPUs and are able to model domains including several million elements. However, a new class of numerical algorithms based on GPUs has been recently proposed.

Almost two decades ago, the numerical performance switched from a compute-bound to memory-bound algorithms, this switch being known as “memory wall”. The most computationally expensive part in modern hardware is reading and writing data from global memory; hundreds of arithmetic operations can be performed per one memory access without limiting performance. Such a revolution accelerated the

development of highly parallel devices to overcome limitations related to reading and writing large amounts of data. Graphical processing units or GPUs are the class of highly parallel devices which allow us to execute thousands of programming instructions in a parallel fashion, and memory bandwidth exceeding that of CPUs by orders of magnitude. The algorithms developed for GPUs are very efficient and can tackle three-dimensional problems with a resolution involving trillions of degrees of freedom (Alkhimenkov et al., 2021b; Räss et al., 2022). We here list several recently developed GPU-based applications. Omlin et al. (2017) performed simulations of reactive solitary waves in three-dimensions. Omlin et al. (2018); Räss et al. (2019) used GPUs to resolve viscoelastic deformation coupled to porous fluid flow. Duretz et al. (2019b) investigated thermomechanical coupling in two and three dimensions. Räss et al. (2020) modeled thermomechanical ice deformation. Alkhimenkov et al. (2021b,a) proposed a multi-graphical wave propagation code for poroelastic media resolving over 1.5 billion grid cells in a few seconds. Finally, Räss et al. (2022) provided an efficient numerical implementation of pseudo-transient iterative solvers on GPUs using the Julia programming language.

Plasticity has a long history and many scientists contributed into this field. Early studies of strain localization in solids include (Hill, 1950, 1958; Kachanov, 1974; Rudnicki and Rice, 1975; Rice and Rudnicki, 1980; Vardoulakis et al., 1978; Vermeer and De Borst, 1984; Sulem and Vardoulakis, 1995). The mechanics of faults and earthquakes is given in a monograph by Scholz (2019). Vermeer (1990) analyzed the possible orientations of shear bands in biaxial tests. Forsyth (1992); Buck (1993) explored the angle of normal faulting. Due to the non-linearity of the problem, numerical modeling of strain localization remains challenging. Cundall (1989, 1990); Poliakov et al. (1993, 1994); Poliakov and Herrmann (1994) are the early studies addressing strain localization in brittle rocks. The modeling of strain localization in visco-plastic rheology was conducted by Kaus and Podladchikov (2006). Kaus (2010) numerically studied the angle of shear bands considering brittle deformation. Spiegelman et al. (2016) explore the algorithms to solve the incompressible equations with visco-plastic rheologies. Glerum et al. (2018) combined plasticity and nonlinear visco-plastic rheology. Regularization of the strain localization thickness was performed by Duretz et al. (2019a) and de Borst and Duretz (2020). Geodynamic modeling of frictional plasticity were performed by Duretz et al. (2020, 2021). Minakov and Yarushina (2021) used a two-dimensional elastoplastic model for microearthquake source generation.

The current understanding of the earthquake nucleation is based on studying of the sliding behavior of frictional surfaces. It is believed that the interseismic period is governed by nearly elastic behavior of the crust with periods of anelastic slip (Pranger et al., 2022). The majority of the modeling studies of earthquake sequences are based on the phenomenological rate- and state-dependent friction law (Dieterich,

1978, 1979; Ruina, 1983). However, new studies of the earthquake nucleation include additional physical mechanisms, such as plasticity, which might be important for proper modeling of earthquake sequences. The effects of off-fault plasticity in 2-D in-plane dynamic rupture simulations was conducted by Templeton and Rice (2008); Kaneko and Fialko (2011); Gabriel et al. (2013); Tong and Lavier (2018); Allison and Dunham (2018). Off-fault plasticity in three-dimensional dynamic rupture simulations was studied by Wollherr et al. (2018). Dal Zilio et al. (2022) presented a 2-D thermomechanical computational framework for simulating earthquake sequences in a non-linear visco-elasto-plastic compressible medium. Uphoff et al. (2023) used a discontinuous Galerkin method for modeling of earthquake sequences and aseismic slip on multiple faults.

We here propose a GPU-based numerical implementation of the compressible and incompressible visco-elasto-plastic inertialess equations in two- and three-dimensions. Similarly to Alkhimenkov et al. (2021b), the present algorithm relies on the three key ideas: concise numerical implementation, high numerical resolution and high computational efficiency. Concise numerical implementation manifests in short and simple numerical code developed for GPU devices. Spatial and temporal discretization is implemented using a conservative staggered grid numerical scheme (Virieux, 1986), equivalent to a variant of a finite-volume method (Dormy and Tarantola, 1995). The solution of the quasi-static problem is achieved using the matrix free pseudo-transient (relaxation) method (Frankel, 1950; Räss et al., 2022) which showed its robustness and scalability in large high-performance computing applications. We rely on the perfect plasticity theory and implement a non-associated pressure-dependent Drucker–Prager criterion (Drucker and Prager, 1952; de Souza Neto et al., 2011). The high numerical resolution involving over 130 million grid cells allows our numerical algorithm to resolve strain localization in two- and three- dimensions. In principle, the resolution is only limited by the available GPU memory and can be up to several billions as it was presented by Alkhimenkov et al. (2021b); Räss et al. (2022). High computational efficiency means that the numerical simulations lasts for several minutes or hours depending on the target numerical resolution. The numerical algorithm is implemented in CUDA C programming language which is suitable for Nvidia GPU devices. The developed algorithm is then applied to model the sequence of stress drops associated with strain localization. Such stress drops can be attributed to spontaneous earthquake nucleation.

The originality of the present study is the following:

1. We utilize the simplest pressure-sensitive ideal plasticity model with constant in time and space static friction coefficient.
2. We resolve a non-symmetric strain localization pattern in two- and three- dimensions.
3. We demonstrate the similarity in patterns of strain localization between elasto-plastic and visco-plastic

rheologies for modeling of strain localization.

4. We propose a new physics-based approach explaining spontaneous stress drops in deforming rocks, with potential applications to modelling the nucleation of earthquakes.
5. We achieve fast computational times using high-resolution models in two- and three-dimensions involving more than 500 million degrees of freedom.

2 Governing Equations

We consider a single-phase compressible flow governed by the inertialess equations with visco-elasto-plastic rheology. We use incremental formulation and implement an objective stress rate measure by applying the Jaumann rate. First, we provide the conservation laws and the constitutive relations of the compressible visco-elasto-plastic inertialess equations. A modification leading to the incompressible visco-elasto-plastic inertialess equations is provided in the following section. Then, we explore the Jaumann derivative and non-associated plasticity implemented in the solver. List of principal notation is given in Table 2.

The model includes equations for conservation of mass, momentum, and closure relations. In this study, we consider only isothermal model setups, thus, we don't include the conservation of energy in the model.

Symbol	Meaning	Unit
σ_{ij}	stress tensor	Pa
p	pressure	Pa
τ_{ij}	stress deviator	Pa
$\dot{\epsilon}_{ij}$	deviatoric strain rate	1/s
v_k	velocity	m/s
ρ	density	kg/m ³
K	bulk modulus	Pa
G	shear modulus	Pa
μ_s	shear viscosity	Pa·s
t	time	s

Table 1: List of Principal Notation

2.1 Conservation laws

The conservation of mass can be formulated as:

$$\frac{\partial \rho}{\partial t} + \nabla \cdot (\rho \mathbf{v}) = 0 \quad \text{or} \quad \frac{\partial \rho}{\partial t} + \nabla_j (\rho v_j) = 0, \quad (1)$$

where ρ is the density, and \mathbf{v} is the velocity. The conservation of linear momentum is

$$\nabla \cdot \boldsymbol{\sigma} + \mathbf{f} = 0 \quad \text{or} \quad \nabla_j \sigma_{ij} + f_i = 0, \quad (2)$$

where f_i is the body forces. The stress tensor is decomposed into bulk (volumetric) and deviatoric components

$$\boldsymbol{\sigma} = -p\mathbf{I} + \boldsymbol{\tau} \quad \text{or} \quad \sigma_{ij} = -p\delta_{ij} + \tau_{ij}, \quad (3)$$

where \mathbf{I} is the second order identity tensor, τ_{ij} is the stress deviator, δ_{ij} is the Kronecker delta and $i, j = \overline{1..3}$. Pressure is defined as

$$p = -\frac{1}{3} \text{tr} \boldsymbol{\sigma} \quad \text{or} \quad p = -\frac{1}{3} (\sigma_{xx} + \sigma_{yy} + \sigma_{zz}), \quad (4)$$

where tr is the trace operator. Using equations (3)-(4), the conservation of linear momentum can be rewritten as

$$\nabla \cdot (\boldsymbol{\tau} - p\mathbf{I}) + \mathbf{f} = 0 \quad \text{or} \quad \nabla_j (\tau_{ij} - p\delta_{ij}) + f_i = 0. \quad (5)$$

2.2 Constitutive equations

In the compressible case, the compressibility for the density is as follows:

$$\rho \frac{Dp}{D\rho} = K. \quad (6)$$

For the incompressible case, the density is constant:

$$\rho = \text{const.} \quad (7)$$

Combining the continuity equation and the relation between density and pressure yields:

$$\frac{1}{K} \frac{Dp}{Dt} = -\nabla_k v_k, \quad (8)$$

where Dp/Dt is the material derivative (explored below), ∇ is del (or nabla) operator and $k = \overline{1..3}$. In the incompressible case, Eq. (8) reduces to the divergence-free condition:

$$0 = -\nabla_k v_k. \quad (9)$$

The strain rate is defined as

$$\dot{\varepsilon}_{ij} = \frac{1}{2} (\nabla_i v_j + \nabla_j v_i) \quad (10)$$

The rheology is Maxwell visco-elasto-plastic, which is characterized by an additive decomposition of the strain rate into an elastic (volumetric and deviatoric), viscous and plastic components ($\dot{\varepsilon}^{vp} = \dot{\varepsilon}^{vis} + \dot{\varepsilon}^{pl}$)

$$\dot{\varepsilon}_{ij} = \dot{\varepsilon}_{ij}^{eb} + \dot{\varepsilon}_{ij}^{ed} + \dot{\varepsilon}_{ij}^{vis} + \dot{\varepsilon}_{ij}^{pl}, \quad (11)$$

where the superscripts \cdot^{eb} , \cdot^{ed} , \cdot^{vis} , \cdot^{pl} denote elastic volumetric (bulk), elastic deviatoric, viscous and plastic parts, respectively. The volumetric (bulk) elastic strain rate is

$$\dot{\varepsilon}_{ij}^{eb} = \frac{1}{3} \nabla_k v_k \delta_{ij}, \quad (12)$$

the deviatoric elastic strain rate is

$$\dot{\varepsilon}_{ij}^{ed} = \frac{1}{2G} \frac{\mathcal{D}\tau_{ij}}{\mathcal{D}t}, \quad (13)$$

the deviatoric viscous strain rate is

$$\dot{\varepsilon}_{ij}^{vis} = \frac{\tau_{ij}}{2\mu_s}, \quad (14)$$

the deviatoric plastic strain rate is

$$\dot{\varepsilon}_{ij}^{pl} = \dot{\lambda} \frac{\partial Q}{\partial \sigma_{ij}}, \quad (15)$$

where $\dot{\lambda}$ is the plastic multiplier and Q is the plastic flow potential. Combining equations (11)-(15), the strain rate can be reformulated as

$$\frac{1}{3} \nabla_k v_k \delta_{ij} + \frac{1}{2G} \frac{\mathcal{D}\tau_{ij}}{\mathcal{D}t} + \frac{\tau_{ij}}{2\mu_s} + \dot{\lambda} \frac{\partial Q}{\partial \sigma_{ij}} = \frac{1}{2} (\nabla_i v_j + \nabla_j v_i) = \dot{\varepsilon}_{ij}. \quad (16)$$

In the limit of infinite viscosity, μ_s , the system of equation becomes the static elasto-plastic model routinely used in solid mechanics (Zienkiewicz and Taylor, 2005). In the limit of infinite elastic moduli, K and G , the system of equation becomes the system of Stokes equations used for creeping low Reynolds number flows in fluid mechanics (Zienkiewicz et al., 2013; Happel and Brenner, 1983).

2.3 Connection to large strain elasticity theory

The inelastic response is modeled by hypoelastic constitutive theory. Hypoelasticity corresponds the formulation of the constitutive equations for stress in terms of objective (frame invariant) stress rates

(de Souza Neto et al., 2011). The rate evolution law for stress is the following (de Souza Neto et al., 2011; De Borst et al., 2012)

$$\frac{\mathcal{D}\boldsymbol{\sigma}}{\mathcal{D}t} = \mathbf{C}^e : \dot{\boldsymbol{\epsilon}}^e = \mathbf{C}^e : (\dot{\boldsymbol{\epsilon}} - \dot{\boldsymbol{\epsilon}}^{vp}), \quad (17)$$

where $\mathcal{D}\tau_{ij}/\mathcal{D}t$ denotes the Jaumann rate of Cauchy stress or simply Jaumann derivative (explored below), \mathbf{C}^e is the tangential elasticity operator, $\dot{\boldsymbol{\epsilon}} = \dot{\boldsymbol{\epsilon}}^e + \dot{\boldsymbol{\epsilon}}^{vp}$ is the strain rate tensor decomposed into elastic $\dot{\boldsymbol{\epsilon}}^e$ and visco-plastic $\dot{\boldsymbol{\epsilon}}^{vp}$ parts. For simplicity, we assume that \mathbf{C}^e is the elasticity tensor. We assume that the medium is isotropic and decompose the total stress tensor into the deviatoric component and pressure. The stiffness tensor C_{ijkl}^e can be fully described by the bulk K and shear G moduli:

$$C_{ijkl}^e = \left(K - \frac{2}{3}G \right) \delta_{ij}\delta_{kl} + 2G \left(\frac{1}{2}(\delta_{ik}\delta_{jl} + \delta_{il}\delta_{kj}) \right), \quad (18)$$

where δ_{ij} is the Kronecker delta. The relation (17) reduces to equation (16) in the compressible case.

2.4 Jaumann rate of stress

The Jaumann rate of Cauchy stress, denoted as $\mathcal{D}\sigma_{ij}/\mathcal{D}t$, is defined as (de Souza Neto et al., 2011)

$$\frac{\mathcal{D}\sigma_{ij}}{\mathcal{D}t} = \frac{\partial\sigma_{ij}}{\partial t} + v_k \frac{\partial\sigma_{ij}}{\partial x_k} \overbrace{-\dot{w}_{ik}\sigma_{jk} - \dot{w}_{jk}\sigma_{ik}}^{-\sigma_{ij}^{\mathcal{R}}}, \quad (19)$$

where \dot{w}_{ij} is the vorticity tensor defined as

$$\dot{w}_{ij} = \frac{1}{2}(\nabla_i v_j - \nabla_j v_i). \quad (20)$$

and $\sigma_{ij}^{\mathcal{R}}$ is the rotation of the Cauchy stress tensor. The Jaumann derivative consists of stress advection and stress rotation terms. Equation (19) can be re-arranged as

$$\frac{\mathcal{D}\sigma_{ij}}{\mathcal{D}t} = \frac{D\sigma_{ij}}{Dt} - \sigma_{ij}^{\mathcal{R}}, \quad (21)$$

where $D/\sigma_{ij}Dt$ is the material derivative:

$$\frac{D\sigma_{ij}}{Dt} = \frac{\partial\sigma_{ij}}{\partial t} + v_k \frac{\partial\sigma_{ij}}{\partial x_k}, \quad (22)$$

and $\sigma_{ij}^{\mathcal{R}}$ is

$$\sigma_{ij}^{\mathcal{R}} = \dot{w}_{ik}\sigma_{jk} + \dot{w}_{jk}\sigma_{ik} \quad (23)$$

Expressions for $\sigma_{ij}^{\mathcal{R}}$ in two- and three-dimensional configuration are given in A. The Jaumann rate of stress deviator τ_{ij} can be calculated using the same expressions (19)-(23) with σ_{ij} replaced by τ_{ij} .

2.5 Plasticity

Plasticity is implemented using a non-associated pressure-dependent Drucker–Prager criterion (Drucker and Prager, 1952; de Souza Neto et al., 2011; De Borst et al., 2012). This criterion states that plastic yielding begins when, the second invariant of the deviatoric stress, J_2 , and the pressure (mean or hydrostatic stress), p , reach the following condition

$$\sqrt{J_2} - Ap = Bc, \quad (24)$$

where A and B are the material parameters determined from experiments, c is the cohesion. In terms of the stress tensor, plastic deformations take place when stresses reach the the yield surface. The yield function F and the plastic potential Q for the Drucker–Prager criterion are defined as

$$F(\tau, p) = \sqrt{J_2} - Ap - Bc, \quad (25)$$

$$Q(\tau, p) = \sqrt{J_2} - Cp. \quad (26)$$

In two-dimensional configuration, $A = \sin(\phi)$, $B = \cos(\phi)$ and $C = \sin(\psi)$, where ϕ is the angle of internal friction and $\psi \leq \phi$ is the dilation angle. Note, that in two-dimensions under plain strain condition, with $\sigma_{zz} = \frac{1}{2}(\sigma_{xx} + \sigma_{yy})$, Drucker–Prager criterion is equivalent to Mohr-Coulumb criterion (Templeton and Rice, 2008). In three-dimensional configuration, expressions for A , B and C are the following

$$A = \frac{6 \sin(\phi)}{\sqrt{3}(3 - \sin(\phi))}, \quad (27)$$

$$B = \frac{6 \cos(\phi)}{\sqrt{3}(3 - \sin(\phi))}, \quad (28)$$

$$C = \frac{6 \sin(\psi)}{\sqrt{3}(3 - \sin(\psi))}, \quad (29)$$

In two dimensions, the second invariant of the deviatoric stress, J_2 , is expressed as

$$J_2 = \frac{1}{2} \boldsymbol{\tau} : \boldsymbol{\tau} = \frac{1}{2} \tau_{ij} \tau_{ji} = \frac{1}{2} (\tau_{xx}^2 + \tau_{yy}^2) + \tau_{xy}, \quad (30)$$

where the symbol $:$ denotes the double dot product. In three-dimensions, J_2 is expressed as

$$J_2 = \frac{1}{2} \boldsymbol{\tau} : \boldsymbol{\tau} = \frac{1}{2} \tau_{ij} \tau_{ji} = \frac{1}{2} (\tau_{xx}^2 + \tau_{yy}^2 + \tau_{zz}^2) + \tau_{xy} + \tau_{xz} + \tau_{yz}, \quad (31)$$

As long as function $F \leq 0$, the material is in elastic regime. Once F reaches a zero value ($F = 0$) plasticity is activated. If the material remains in plastic state ($\partial F / \partial t = 0$) plastic yielding occurs. The present implementation of perfect plasticity requires small temporal increments and is computationally expensive. In our formulation, we assume that the dilation angle $\psi = 0$. Thus, the plastic multiplier $\dot{\lambda}$ has a simple form

$$\dot{\lambda} = \frac{Ap + Bc}{\sqrt{J_2}}. \quad (32)$$

One way to guaranty spontaneous strain localization is to introduce some form of strain softening that is widely used to ensure formation of the shear bands (Lavie et al., 1999; Moresi et al., 2007a; Popov and Sobolev, 2008; Lemiale et al., 2008). However, there are concerns about thermodynamic admissibility of such solutions (Duretz et al., 2019a). Moreover, softening or hardening modulus are small compared to shear modulus and can be neglected as a first-order approximation leading to the ideal plasticity model used in the present study.

2.6 Summary of the governing equations

Simulations can be conducted by solving the following equations for pressure p , stress deviator τ_{ij} and velocities v_k :

$$\nabla_j (\tau_{ij} - p \delta_{ij}) = 0, \quad (33)$$

$$\frac{1}{K} \frac{Dp}{Dt} = -\nabla_k v_k, \quad (34)$$

$$\frac{1}{2G} \frac{D\tau_{ij}}{Dt} + \frac{\tau_{ij}}{2\mu_s} + \dot{\lambda} \frac{\partial Q}{\partial \sigma_{ij}} = \frac{1}{2} (\nabla_i v_j + \nabla_j v_i) - \frac{1}{3} \nabla_k v_k \delta_{ij}. \quad (35)$$

In 2D, we have 6 unknowns ($p, \tau_{xx}, \tau_{yy}, \tau_{xy}, v_x, v_y$) and 6 equations. In 3D, we have 10 unknowns ($p, \tau_{xx}, \tau_{yy}, \tau_{zz}, \tau_{xy}, \tau_{xz}, \tau_{yz}, v_x, v_y, v_z$) and 10 equations, respectively.

2.6.1 Nondimensionalization

We choose the following dimensionally independent scales: length $l^* = L_x$, time $t^* = 1/a$ and pressure $p^* = G_0$. L_x is the size of the computational domain in x -dimension, a is the background strain rate. After rescaling, the model is defined by 4 non-dimensional numbers summarized in the Table 3.

The deformation occurs at times inversely proportional to the background strain rate a_0 at time $t = 0$. Deborah number De characterises the ratio between and the Maxwell relaxation time η/G_0 and the characteristic time of deformation t^* . Thus, if $De \gg 1$, the deformation occurs at much shorter time scales than stress relaxation, corresponding to brittle-like behavior (elastic domain). Conversely, if $De \ll 1$, the stress relaxation is much faster than the deformation, corresponding to the fluid-like, or ductile, behavior (viscous domain). In the ductile regime, high strain rates are necessary to build up stresses sufficient for plastic deformation. ν is the Poisson's ratio characterising relative effect of compressibility. r characterises the ratio between cohesion c and the pressure scale p^* .

Scale	Meaning
$l^* = L_x$	Domain size in x -direction
$t^* = \frac{1}{a}$	time
$p^* = G_0$	pressure

Table 2: Independent scales

Dimensionless number	Meaning
$De = a_0 \frac{\eta}{G_0}$	Deborah
$\nu = \frac{3K - 2G_0}{2(3K - G_0)}$	Poisson's ratio
$r = \frac{c_0}{G_0}$	cohesion to pressure scale
$\gamma = \frac{da}{dt} t^{*2}$	increment of strain rate

Table 3: Dimensionless parameters

3 Numerical solution strategy

3.1 Discretization

The model domain is discretized using a regular time-space grid. A solution of the system (33)-(35) is performed using a conservative staggered space-time grid discretization (Virieux and Madariaga, 1982; Virieux, 1986). In this approach, fluxes are calculated at the cell boundaries whereas field variables are located at either at cell centers or corners. As a result, a conservative scheme space-time numerical scheme is achieved, which is equivalent to a finite volume method (Dormy and Tarantola, 1995; LeVeque, 1992). The current configuration of the staggered space-time grid discretization is provided in Alkhimenkov et al. (2021b); a review of the explicit staggered grid approach is given by Moczo et al. (2007).

3.2 Accelerated pseudo-transient method

An iterative matrix-free pseudo-transient method (Frankel, 1950; Räss et al., 2022) is used to obtain the solution of the quasi-static problem. The pseudo-transient method is a physics-inspired iterative method that solves the quasi-static equations by adding a pseudo-time derivative, through which the steady-state solution is progressively achieved via a pseudo-time stepping. In other words, the quasi-static solution is an attractor of the dynamic equation (with inertia) with a pseudo-time derivative. This method is also known as the relaxation method (Frankel, 1950).

A steady-state solution of the given system of equations (33)-(35) can be performed by converting the equations into a pseudo-transient formulation in two steps: (i) adding inertia term with a "pseudo" time step \tilde{t} into the momentum equation and (ii) adding Maxwell type viscous rheology into the constitutive equation. The pseudo-transient version of the momentum equation is

$$\tilde{\rho} \frac{\partial v_i}{\partial \tilde{t}} = \nabla_j (\tau_{ij} - p \delta_{ij}) + f_i \quad (36)$$

In compressible case, the pseudo-transient version of the equation for pressure (8) becomes:

$$\frac{1}{\tilde{K}} \frac{\partial p}{\partial \tilde{t}} + \frac{1}{K} \frac{p - \hat{p}}{\Delta t} = -\nabla_k v_k \quad (37)$$

In incompressible case, the pseudo-transient version of equation (9) becomes:

$$\frac{1}{\tilde{K}} \frac{\partial p}{\partial \tilde{t}} = -\nabla_k v_k \quad (38)$$

For the stress deviator the corresponding equation is

$$\frac{1}{2\tilde{G}} \frac{\partial \tau_{ij}}{\partial t} + \frac{1}{2G} \frac{\tau_{ij} - \hat{\tau}_{ij}}{\Delta t} + \frac{\tau_{ij}}{2\mu_s} = -\lambda \frac{\partial Q}{\partial \sigma_{ij}} + \frac{1}{2} \left(\nabla_i v_j + \nabla_j v_i - \frac{2}{3} \nabla_k v_k \right). \quad (39)$$

The only difference between the pseudo-transient versions of compressible and incompressible equations is the equation for pressure (equation (37) or (38)), all other equations remain the same.

In (36), (37), (39), the quantities \tilde{K} , \tilde{G} and $\tilde{\rho}$ are to be determined numerical parameters. Räss et al. (2022) showed that the optimal values of the numerical parameters for the incompressible visco-elastic inertialess equation are

$$\tilde{\rho} = \tilde{Re} \frac{\mu_s}{VL}, \quad (40)$$

$$\tilde{G} = \frac{\tilde{\rho} \tilde{V}^2}{r + \frac{4}{3}}, \quad (41)$$

$$\tilde{K} = r\tilde{G}, \quad (42)$$

where $r = \tilde{K}/\tilde{G}$, $\tilde{Re} = \tilde{\rho}V_pL/\mu_s$ is the numerical Reynolds number and the primary, or P-wave, velocity is

$$V_p = \sqrt{\frac{\tilde{K} + \frac{4}{3}\tilde{G}}{\tilde{\rho}}}. \quad (43)$$

Only two numerical parameters, \tilde{Re} and r , control the convergence of the pseud-transient method. A one-dimensional dispersion analysis for the incompressible visco-elastic equation provide us with the following optimal values (Räss et al., 2022)

$$\tilde{Re}_{opt} = \frac{3\sqrt{10}}{2}\pi, \quad (44)$$

$$r_{opt} = \frac{1}{2}. \quad (45)$$

Numerical tests in two- and three- dimensions show that the derived values for \tilde{Re}_{opt} and r_{opt} remain valid for the compressible visco-elastic equation as well.

3.3 Return mapping algorithm for plasticity

In the return mapping algorithm, once the trial deviatoric stress reaches the value of $\bar{c} = Ap + Bc$, the deviatoric updated stress is obtained by simply scaling down the trial deviatoric stress by a factor that depends on $\Delta\lambda$ and is defined by equation (32). In two- and three- dimensional large scale numerical simulations involving more than 1 million grid cells, we used the concept of the "frozen" plasticity. If after $16 \times n_x$ iterations (n_x - number of cells in x -dimension) for a given time step (increment), the relative error ϵ_{rel} (eq. (54)) is larger than 10^{-4} , we stop updating $\dot{\lambda}$ (i.e., we "freeze" plastic multiplier) and iterate until the solution is converged to the desired tolerance ϵ_{rel} .

3.4 The CUDA C implementation using graphical processing units (GPUs)

We use the CUDA C language to implement the numerical solver. The solver consists of two time loops: the first time loop belongs to physical time t whereas the second time loop belongs to the pseudo-time \tilde{t} integration to achieve a steady-state solution at each discrete physical time step. Figure 1 shows the time loop computations of compressible visco-elasto-plastic solver for a single GPU CUDA C code implementation. The time loops call several kernels (GPU functions) to sequentially solve the system of equations (33)-(35).

We calculated our results using several computing systems. The code prototyping was developed on a laptop hosting 13th Gen Intel Core i9-13900HX CPU (64GB RAM) and NVIDIA GeForce RTX 4090 (16GB) laptop GPU. Large scale two- and three- dimensional simulations were conducted on an NVIDIA DGX-1 - like node hosting 4 NVIDIA Ampere A100 (80GB) GPUs and AMD EPYC 7742 (512GB RAM) Server Processor.

4 Modeling Results

4.1 Model Configuration and Boundary conditions

The visco-elasto-plastic solver is represented by the system of equations (33)-(35). The computational domain is a cube (or square in 2D) with dimensions $x, y, z \in [0, L_x] \times [0, L_y] \times [0, L_z]$ (in 2D $x, y \in [0, L_x] \times [0, L_y]$). All simulations presented in this study have been performed using a simple initial model configuration. The pure shear boundary conditions are applied by prescribing velocities at all boundaries. In two-dimensions, we set

$$v_x = ax \tag{46}$$

and

$$v_y = -ay, \quad (47)$$

In three-dimensions, we prescribe

$$v_x = ax, \quad (48)$$

$$v_y = -ay, \quad (49)$$

and

$$v_z = 0, \quad (50)$$

which corresponds to the extension in x-dimension and compression in y- dimension. In the brittle regime (elastic domain), we impose loading increments applied to the strain components. In the ductile regime (viscous domain), we impose velocity increments. At all boundaries, free-slip boundary conditions are implemented.

We introduce the non-dimensional shear modulus and non-dimensional cohesion:

$$\bar{G} = G/G_0, \quad (51)$$

$$\bar{c} = c/c_0. \quad (52)$$

In all simulations, except for the first series of computations (section "Symmetry versus non-symmetry"), the following initial conditions and heterogeneities are employed. All initial conditions (pressure, deviatoric stress and strain) are set equal to zero. We set anomalies to the non-dimensional shear modulus \bar{G} and cohesion \bar{c} . The shear modulus \bar{G} is represented by a Gaussian distribution with the lowest value ($\bar{G} = 1$) attributed to the center of the model, \bar{G} gradually increases towards the walls of the model reaching the highest value of $\bar{G} = 1.2$. The non-dimensional cohesion \bar{c} has a similar Gaussian distribution with the lowest value ($\bar{c} = 0.2 \cdot 10^{-2}$) in the center of the model; in addition, a sharp jump to the higher value ($\bar{c} = 0.4 \cdot 10^{-2}$) is introduced near the walls of the model to eliminate possible boundary effects. The angle of internal friction is $\phi = 30^\circ$ in all computations.

4.2 Convergence study

We use L^∞ metric space for measuring the error:

$$L^\infty(\mathbf{V}) = \max_i |V_i| \quad (53)$$

The relative error is calculated as

$$\epsilon_{\text{rel}} = \frac{\max_i \{|V_i - V_i^{it}\}|}{\max_i \{|V_i|\}} \quad (54)$$

and the residual equation error is

$$\epsilon_{\text{abs}} = \max_i \{|-\nabla p_i + \nabla \cdot \boldsymbol{\tau}_i|\}. \quad (55)$$

Figure 2 shows a typical evolution of the relative L^∞ norm of residuals throughout the localization phase. The relative residual error ϵ_{rel} for a (typical) 10^{th} strain increment of a simulation involving 1535×767 cells is shown in Figure 2a. The absolute residual error ϵ_{abs} for the same simulation is shown in Figure 2b.

4.3 Symmetry versus non-symmetry

The first series of computations are carried using compressible visco-elasto-plastic equations. The Deborah number is set to $De = 10^6$ which corresponds to the brittle domain (elastic limit). We set a circular pressure anomaly to the center of the model ($p = \bar{c}/2$ inside the perturbation, $p = 0$ outside the perturbation). We set the shear modulus $\bar{G} = 1$ and the cohesion $\bar{c} = 0.2 \cdot 10^{-2}$ in the entire model domain. Figure 4ae shows the integrated stress over one vertical line segment versus time. Figure 4bc shows the second invariant of the accumulated strain ϵ_{II} for two different temporal resolutions.

First, we run two low-resolution simulations of 383×191 grid cells. Note that in this example, for simplicity, we exclude the Jaumann derivative. In the first run, only 7 increments in time were performed (with a large time step) (Figure 4b). At each time increment we fully converged to the desired relative error ϵ_{rel} of 10^{-12} (equation (54)). Four shear bands evolve starting from the pressure anomaly and grow towards the walls of the model. An incorrect symmetric strain localization pattern is clearly visible. Contrary, Figure 4c corresponds to the calculation of 180 increments in time (with a small time step), at each increment the iterations converged to the desired relative error ϵ_{rel} of 10^{-12} . Two shear bands develop starting from the pressure anomaly and grow towards the walls of the model, than reflect. The resulting solution exhibits a correct non-symmetric strain localization pattern. Note, that the non-symmetric solution corresponds to

the sharper stress drop (and lower stress) than the symmetric solution (Figure 4a). To further investigate the difference, we plot the displacement increments corresponding to the stress drop $\Delta u_x = u_x(2) - u_x(1)$ for both, symmetric and non-symmetric solutions (Figure 4fg). Sharp discontinuances observed in both solutions. Note that we observe stress drops in deforming medium even without material strain softening or dynamic reduction of the static friction coefficient.

In this set of experiments, we investigate both the temporal and spatial resolutions, as well as, the Jaumann derivative. Figure 5 shows the integrated stress over one vertical line segment versus the number of increments and the second invariant of the accumulated strain ε_{II} for different temporal and spatial resolutions. Two to four shear bands develop starting from the pressure anomaly (Figure 5bdfh). First, we run a low-resolution simulation of 191×95 grid cells, 8 increments in total (Figure 5b). At each time increment we fully converged to the desired relative error ϵ_{rel} of 10^{-12} . A symmetric strain localization pattern is clearly visible. Then, we run a simulation for the resolution of 383×191 grid cells, 8 increments in total (Figure 5d). At each time increment we fully converged to the desired relative error ϵ_{rel} of 10^{-12} . Again, a symmetric strain localization pattern can be observed. For the next simulation, we increased the temporal resolution by increasing the number of loading steps (i.e., by decreasing the time step) and performed 180 increments. At each increment the simulation converged to the desired relative error ϵ_{rel} of 10^{-12} . As a result, a correct non-symmetric strain localization pattern is visible (Figure 5f). Note, that the stress drop is also visible in Figure 5e compared to previous simulations in Figures 5ac. In a similar way, we performed a simulation of 1535×767 grid cells and kept the same temporal resolution. Again, a correct non-symmetric strain localization pattern (Figure 5h) as well as the stress drop (Figure 5g) are visible.

```

for (it=0;it<nt;it++){

    compute_old<<<grid,block >>> (Vx_d, Vy_d, Vz_d, Pt_d, Txx_d, Tyy_d, Tzz_d, ...);

    eta_ve = (DAT)1.0 / ((DAT)1.0 / eta + (DAT)1.0 / (G * dt));
    dt_rho = Vpdt * Lx * ((DAT)1.0 / (Re * eta_ve));
    Gdt = Vpdt * Vpdt * ((DAT)1.0 / (dt_rho * (K_G + (DAT)4.0 / (DAT)3.0)));
    Kdt = K_G * Gdt;
    Kr = Kdt / (K * dt);
    int Dyn = 0;
    cudaDeviceSynchronize();

    adv1 <<< <grid, block >>> (Vx_d, Vy_d, Vz_d, Pt_d, Txx_d, Tyy_d, Tzz_d, ...);
    adv2 <<< <grid, block >>> (Vx_d, Vy_d, Vz_d, Pt_d, Txx_d, Tyy_d, Tzz_d, ...);
    cudaDeviceSynchronize();
    cudaDeviceSynchronize();

    jaumannD <<< <grid, block >>> (Vx_d, Vy_d, Vz_d, Pt_d, Txx_d, Tyy_d, Tzz_d, ...);
    jaumannD2 <<< <grid, block >>> (Vx_d, Vy_d, Vz_d, Pt_d, Txx_d, Tyy_d, Tzz_d, ...);
    cudaDeviceSynchronize();
    cudaDeviceSynchronize();

    compute_old2 <<< <grid, block >>> (Vx_d, Vy_d, Vz_d, Pt_d, Txx_d, Tyy_d, Tzz_d, ...);
    iter = 0; resid = (DAT)2.0 * epsi;
    while (iter < niter && resid>epsi) {

        compute_Stress <<< <grid, block >>> (Vx_d, Vy_d, Vz_d, Pt_d, Txx_d, Tyy_d, Tzz_d, ...);
        cudaDeviceSynchronize();

        compute_BC1 <<< <grid, block >>> (Vx_d, Vy_d, Vz_d, Pt_d, Txx_d, Tyy_d, Tzz_d, ...);
        compute_BC2 <<< <grid, block >>> (Vx_d, Vy_d, Vz_d, Pt_d, Txx_d, Tyy_d, Tzz_d, ...);
        cudaDeviceSynchronize();
        cudaDeviceSynchronize();

        compute_Stress2 <<< <grid, block >>> (Vx_d, Vy_d, Vz_d, Pt_d, Txx_d, Tyy_d, Tzz_d, ...);
        cudaDeviceSynchronize();

        if (iter < (30 * nx + 1) ) {
            compute_V0 <<< <grid, block >>> (Vx_d, Vy_d, Vz_d, Pt_d, Txx_d, Tyy_d, Tzz_d, ...);
            compute_V <<< <grid, block >>> (Vx_d, Vy_d, Vz_d, Pt_d, Txx_d, Tyy_d, Tzz_d, ...);
            cudaDeviceSynchronize();
            cudaDeviceSynchronize();
        }
        if ((iter > (30 * nx) ) && (iter < 500000) ) {
            compute_V0stop <<< <grid, block >>> (Vx_d, Vy_d, Vz_d, Pt_d, Txx_d, Tyy_d, Tzz_d, ...);
            compute_V <<< <grid, block >>> (Vx_d, Vy_d, Vz_d, Pt_d, Txx_d, Tyy_d, Tzz_d, ...);
            cudaDeviceSynchronize();
            cudaDeviceSynchronize();
        }
        if ((iter > (30 * nx) ) && (resid > 1e-4) ) {
            if ((Dyn == 0) ) {
                printf("> Dynamic > iter=%05d , ||resid||=%6.2e ", iter, resid); fflush(stdout);
                Dyn = 1;
            }
        }
        compute_V2 <<< <grid, block >>> (Vx_d, Vy_d, Vz_d, Pt_d, Txx_d, Tyy_d, Tzz_d, ...);
        cudaDeviceSynchronize();

        if ((iter % nout) == 1 ) {
            __MPI_max(Vydif); err_Vydif_MAX = device_MAX; __MPI_max(Vy); err_Vy_MAX = device_MAX;
            resid = (err_Vydif_MAX / err_Vy_MAX);
        }
        iter = iter + 1;
        cudaDeviceSynchronize();
    }
}

```

Figure 1: Time loop computations of compressible visco-elasto-plastic solver for a single GPU CUDA C code implementation. DAT is a shortcut for the double precision. Kernels `adv1` and `adv1` denote the advection. Kernels `jaumannD` and `jaumannD2` correspond to the stress rotation. Kernels `compute_old` and `compute_old2` stand for saving and exchanging values between current and previous time step variables. Kernels `compute_Stress` and `compute_Stress2` correspond to the update of all stresses. Kernels `compute_BC1` and `compute_BC2` stand for boundary conditions. Kernels `compute_V0` and `compute_V` stand for plasticity update (kernel `compute_V0stop` corresponds to the "frozen" plasticity). Kernel `compute_V2` corresponds to the update of velocities.

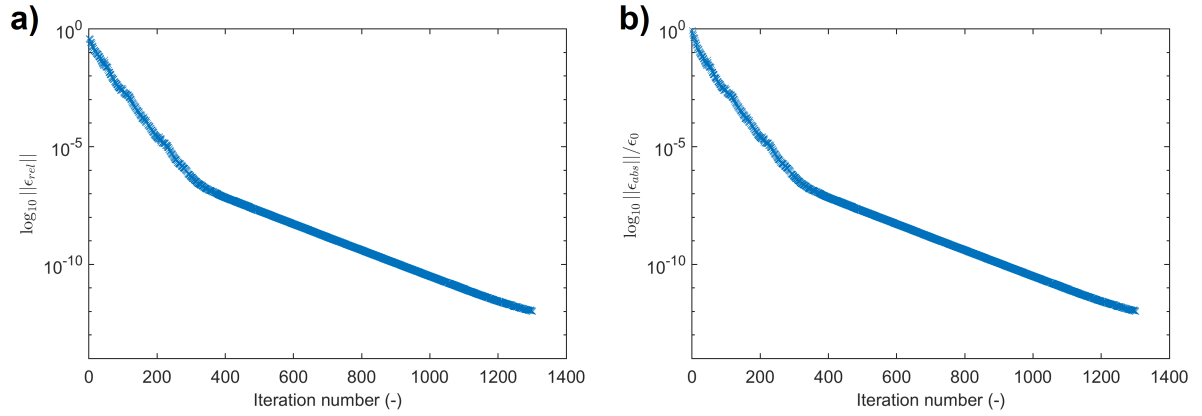


Figure 2: Evolution of the relative L^∞ norm of residuals throughout the localization phase. The model configuration was computed using 1535×767 cells. Panel (a) shows the relative residual error ϵ_{rel} for a (typical) 10^{th} strain increment. Panel (b) shows the absolute residual error ϵ_{abs} for a (typical) 10^{th} strain increment.

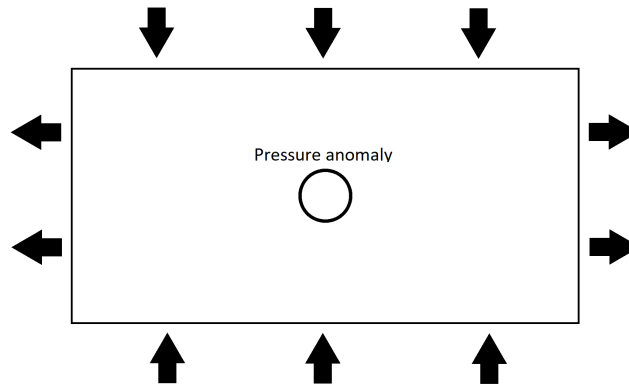


Figure 3: Model configuration. The arrows indicate the pure shear boundary condition which is applied at the model boundaries.

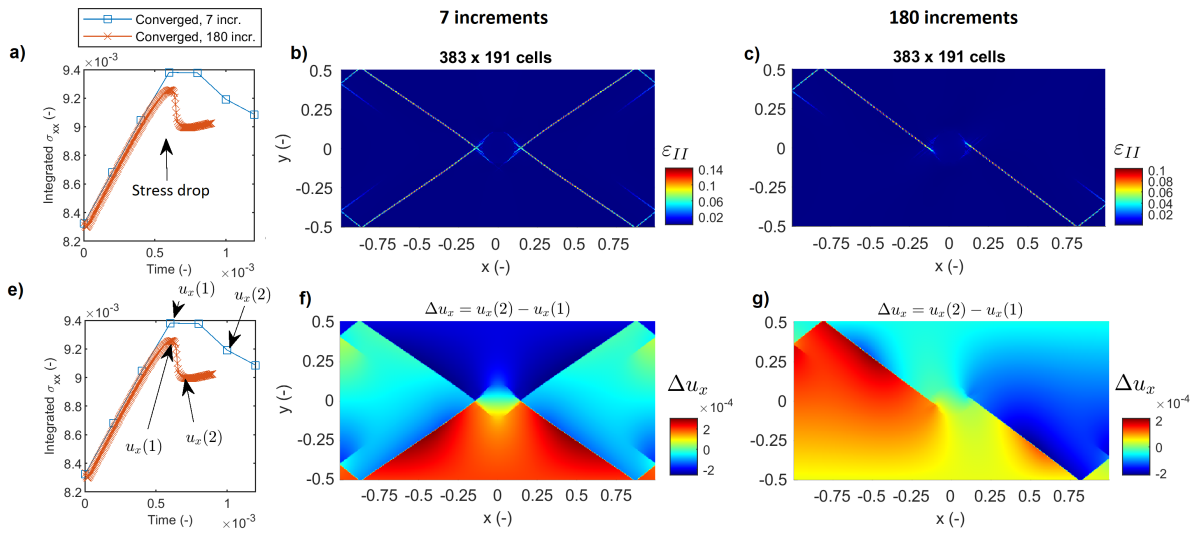


Figure 4: Fully converged solutions without Jaumann derivative. Integrated stress over one vertical line segment versus the number of increments (panels ae), the second invariant of the accumulated strain ε_{II} for different temporal and spatial resolutions (panels bc) and the incremental displacement Δu corresponding to the stress drop (panels fg). Note the non-symmetric pattern of ε_{II} and Δu corresponding the solution with small increments.

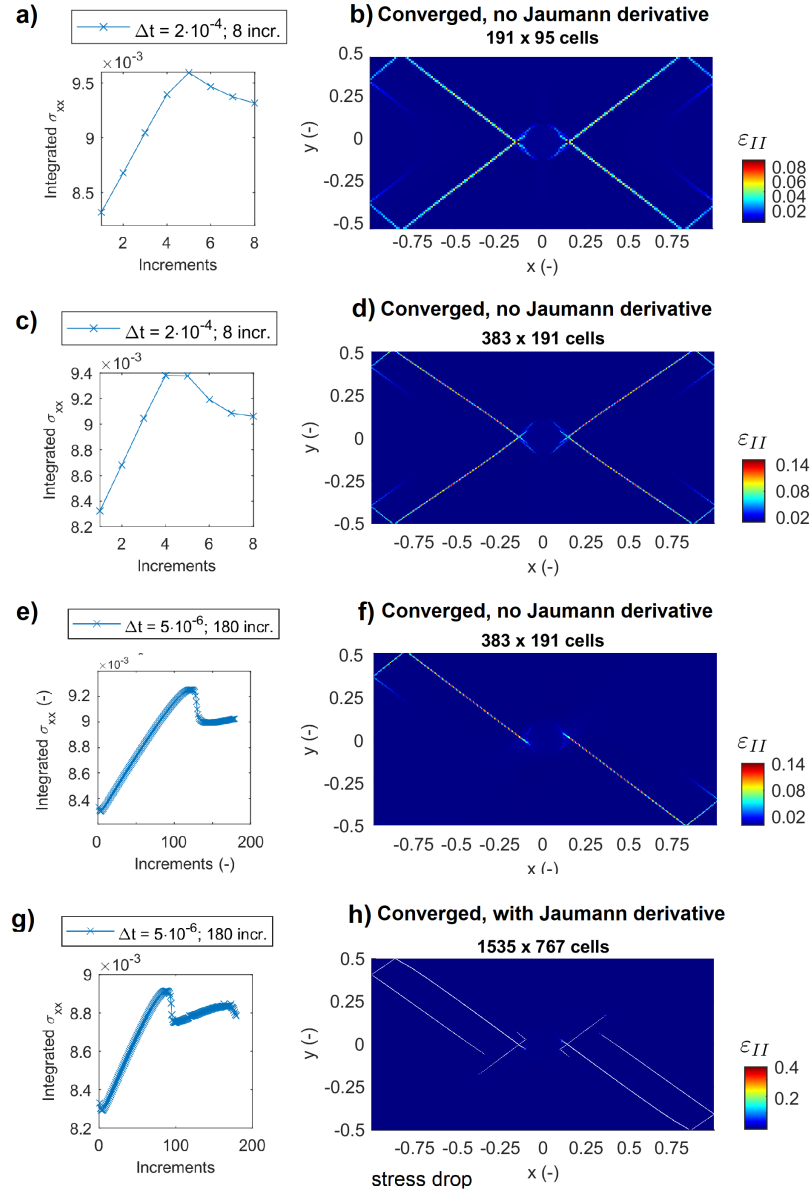


Figure 5: Integrated stress over one vertical line segment versus the number of increments (panels acegi) and the second invariant of the accumulated strain ε_{II} (panels bdfhj) for different temporal and spatial resolutions.

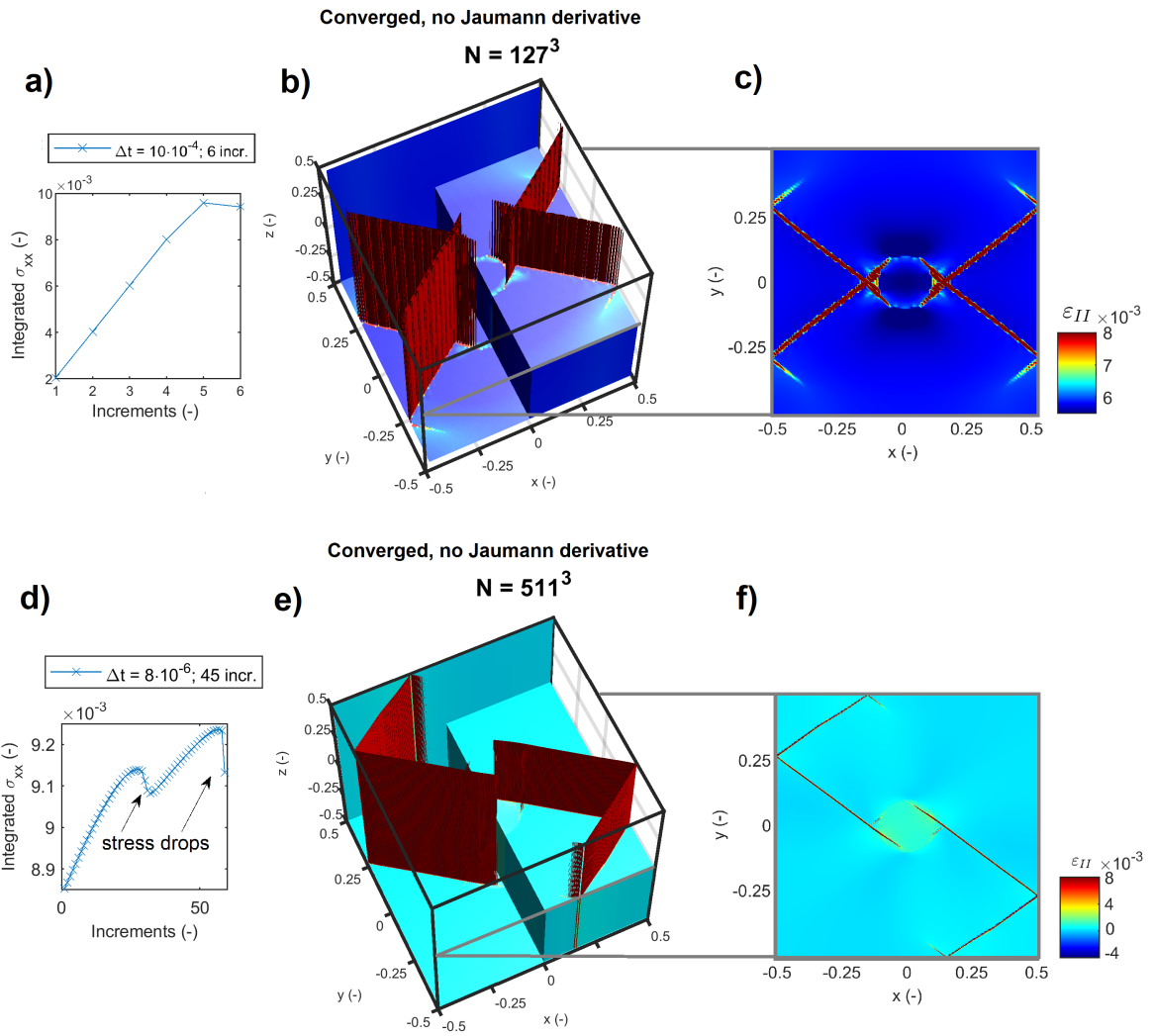


Figure 6: Three-dimensional simulation: integrated stress over one vertical line segment versus the number of increments (panels ad) and the second invariant of the accumulated strain ε_{II} (panels bcef).

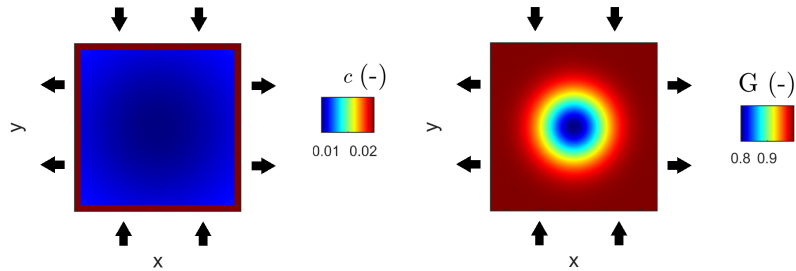


Figure 7: Heterogeneous initial setup of cohesion \bar{c} (left) and shear modulus \bar{G} (right). The arrows indicate the pure shear boundary condition which is applied at the model boundaries.

4.4 Incompressible elastic and viscous limits

In the second set of simulations, we explore the incompressible elastic and viscous limits of the incompressible visco-elasto-plastic equations. Figure 7a shows the initial setup for cohesion, \bar{c} ; shear modulus, \bar{G} , has a constant value of 1. By setting the Deborah number to the high values $De = 10^6$, we reach the elastic limit (brittle domain). Figure 8a-c shows the accumulated strain ε_{II} , the velocity field in x -direction v_x and pressure p for the model configuration corresponding to the elastic limit after 30 loading increments with $\Delta t = 0.4 \cdot 10^{-5}$. The model resolution is $N = 511^2$ grid cells. The strain localization develops at the center of the model with one initial shear band. The shear band is growing towards the walls of the model as the strain increments evolve in physical time. The velocity field v_x clearly shows a discontinuity along the shear band (Figure 8b).

Alternatively, by setting the Deborah number to the low value $De = 10^{-4}$, the viscous limit is reached (ductile domain). Figure 8d-f shows the accumulated strain ε_{II} , the velocity field in x -direction v_x and pressure p after 10 loading increments applied to velocity with $a = 1.01$. As in the elastic limit, the velocity field v_x exhibits a discontinuity along the shear band (Figure 8e). The behavior of the strain localization evolution is similar in both, elastic and viscous, regimes. The only difference between regimes is that in the elastic domain the strain increments are prescribed (equivalent to increments in displacement) whereas in the viscous domain velocity increments are prescribed.

4.5 Targeting high resolution computations

Figure 9 shows the simulation results of compressible visco-elasto-plastic equations in the brittle domain after 10 loading increments with $\Delta t = 0.2 \cdot 10^{-5}$. The model resolution is $N = 10239^2 \approx 105.000.000$ grid cells. Figure 7 shows the initial setup for cohesion, \bar{c} , and shear modulus, \bar{G} . The accumulated strain ε_{II} , the displacement in x -direction u_x and pressure p are shown. Similarly to the previous simulations

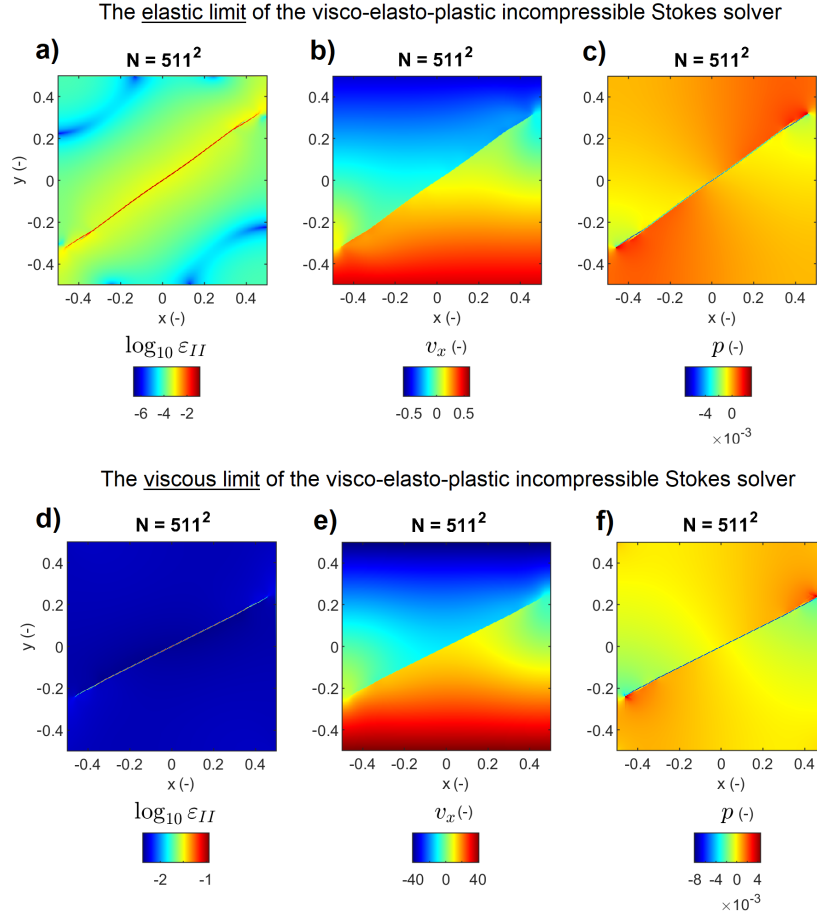


Figure 8: Spatial distribution of accumulated strain ε_{II} , velocity v_x and pressure p fields calculated using an incompressible visco-elasto-plastic equations. Panels (a)-(c) correspond to the elastic limit (brittle domain), panels (d)-(f) correspond to the viscous limit (ductile domain).

of incompressible equations, a single shear band can be observed. However, the orientation is different; according to our numerical experiments, the orientation might be different for any model configuration. It is clearly visible, that the shear band grows under two different angles with a sharp discontinuity between them.

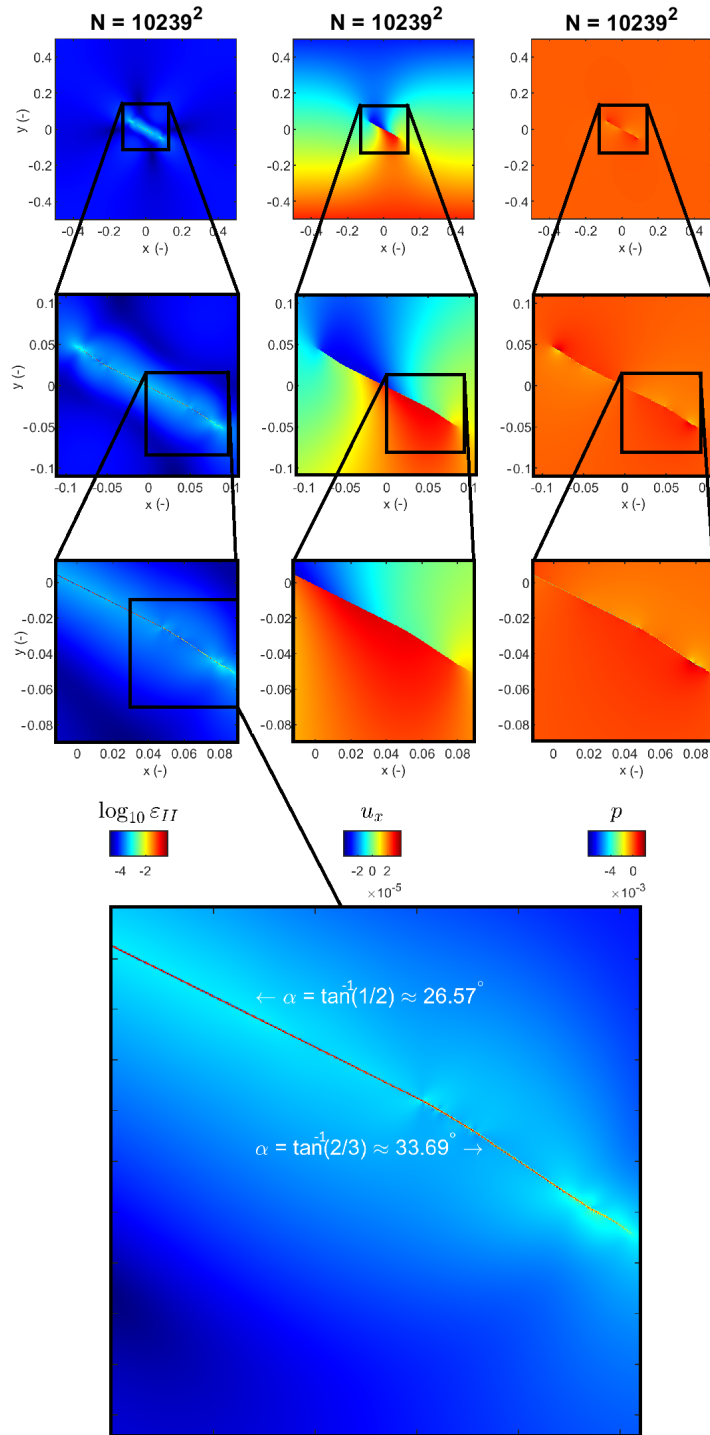


Figure 9: Spatial distribution of accumulated strain ε_{II} , displacement u_x and pressure p fields calculated using compressible visco-elasto-plastic equations. The model resolution is $N = 10239^2 \approx 105,000,000$ grid cells.

4.6 Stress drops in two-dimensional simulations

4.6.1 Convergence tests for a single stress drop

First, we run a temporal resolution test (Figures 10a-d). The spatial resolution is $N = 511^2$ grid cells, simulations with 15, 30, 60, 240 loading increments are performed. Figure 7 shows the initial setup for cohesion, \bar{c} , and shear modulus, \bar{G} . Note that the integrated stress σ_{xx} evolution with loading increments is different depending on the temporal discretization (Figure 10a). The simulations with finer temporal discretization lead to sharper drops in σ_{xx} and lower minimum values of stress σ_{xx} . To further investigate the convergence, we plot the minimum of σ_{xx} versus the number of increments in time (Figure 11). As a result, the minimum of σ_{xx} converges to a constant value as temporal resolution increases.

Figure 10e-h shows the integrated stress σ_{xx} versus time (Figure 10a) and the accumulated strain ε_{II} for a set of different spatial discretizations of $N = 1023^2$, $N = 511^2$ and $N = 383^2$ grid cells (Figure 10f-h). A difference in the integrated stress σ_{xx} evolution is visible. Note, that the minimum value of the integrated stress σ_{xx} is similar for all resolutions.

To further investigate the dependence of the integrated stress σ_{xx} versus temporal resolution, a number of longer simulations were conducted where the second stress drop is visible (Figure 12). The evolution of the integrated stress σ_{xx} around the second stress drop slightly depends of the temporal resolution, however, the difference between simulations of fine resolution is small. The simulation with large loading increments (green curve) significantly diverges from other simulations and don't show stress drops.

4.6.2 Stress drop sequence

Figure 13 shows the integrated stress σ_{xx} versus time (Figure 13a) and the accumulated strain ε_{II} at three discrete loading steps (highlighted by red arrows in Figure 13a). Stress drops have different magnitudes and show non-regular spacing. Stress drops are associated with intersections of shear bands and/or also take place when shear band reaches the higher cohesion values near the boundaries of the model domain.

4.6.3 Interseismic period and stress drops

Figure 14 shows the integrated stress σ_{xx} versus loading increments (Figure 14a) and the displacement increments Δu_x corresponding to the interseismic period (Figure 14b-d) and to the stress drops (Figure 14e-g). For example, Figure 14b shows the displacement increment $\Delta u_x = u_x(2) - u_x(1)$, where $u_x(1)$ and $u_x(2)$ are the displacement fields at the beginning and at the end of the interseismic period (the period between two high-amplitude stress drops, see Figure 14a). Figure 14cd are similar and correspond

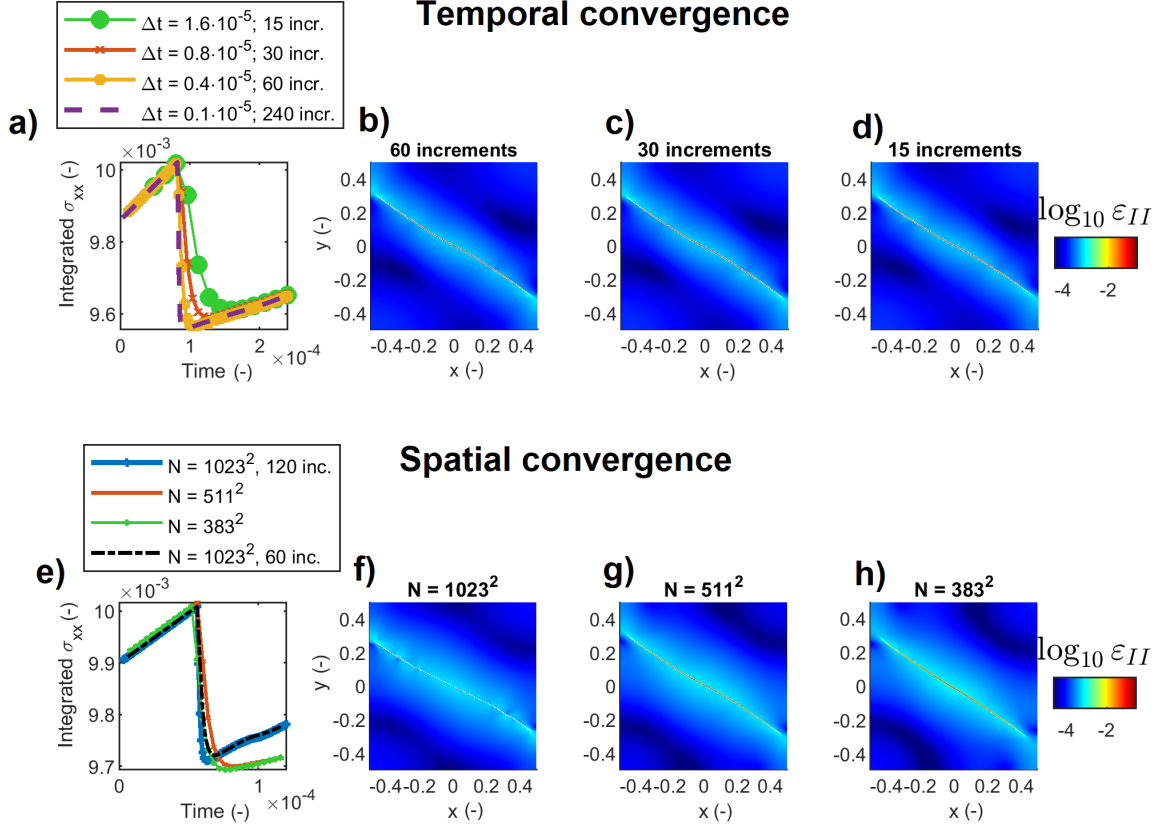


Figure 10: Convergence tests for a single stress drop. Panels (a) and (e) show the integrated stress σ_{xx} versus time, panels (b-d) show the accumulated strain ε_{II} for a set of different temporal discretizations ($N = 511^2$ grid cells) and panels (f-h) show the accumulated strain ε_{II} for a set of different spatial discretizations.

to different interseismic periods. In a similar way, the displacement increment $\Delta u_x = u_x(2) - u_x(1)$ of major stress drops are shown (Figure 14e-g). It can be seen that displacement accumulates during the interseismic period (without major stress drops) and displacement also accumulates during major stress drops but with increased intensity.

4.6.4 Earthquake nucleation due to a single stress drop

Figure 15 shows the integrated stress σ_{xx} versus loading increments (from 2070 to 2170, Figure 15a) and the wave fields (velocity v_x and pressure p) at the initial stage (Figure 15b-c) and after 250 physical time steps (Figure 15d-e). The wavefield pattern at the initial stage is complex and requires further analysis. The volumetric response is of low amplitude (Figure 15ce) while the velocity field produce high amplitudes (Figure 15bd) meaning that shear component exhibits high amplitudes.

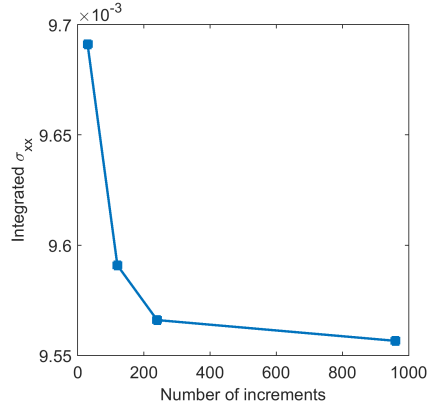


Figure 11: The minimum of the integrated stress σ_{xx} versus the number of loading increments in time.

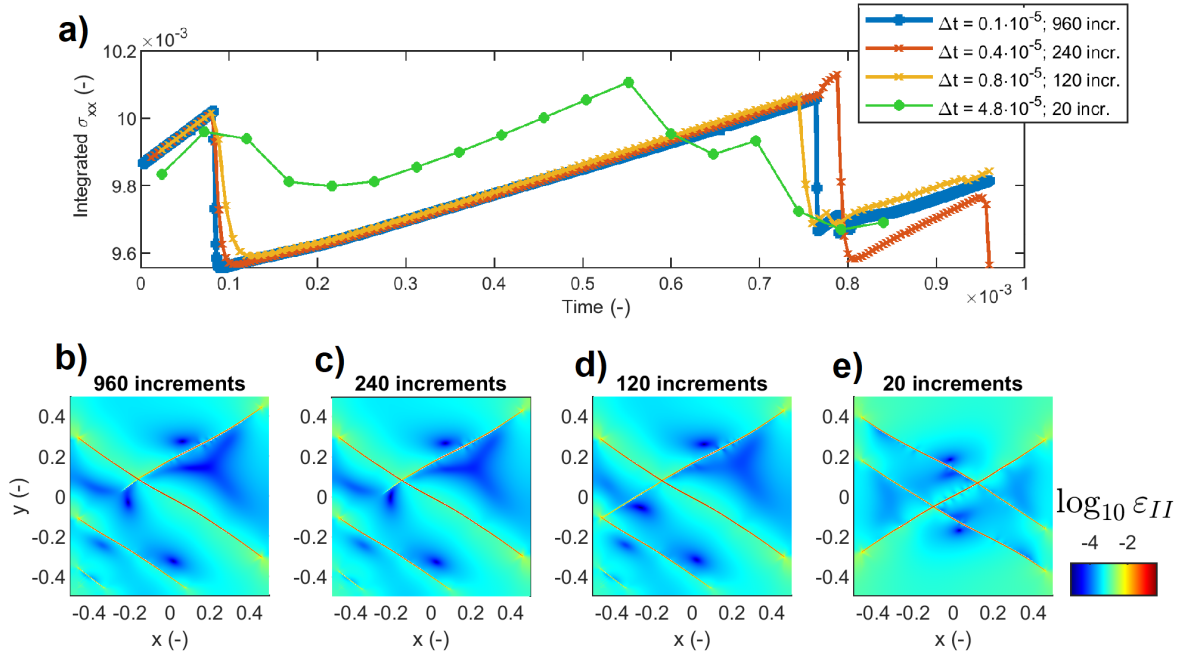


Figure 12: Temporal resolution convergence test. Panel (a) shows the integrated stress σ_{xx} versus time (loading increments), panels (b-e) show the accumulated strain ε_{II} for a set of different temporal discretizations.

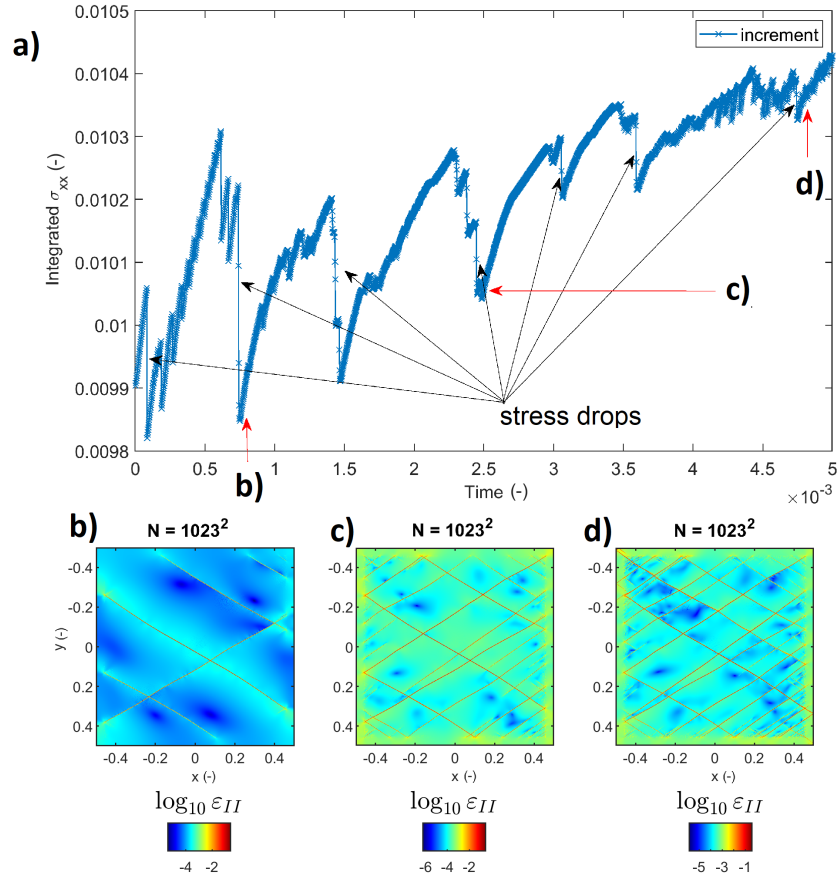


Figure 13: Numerical simulation of compressible visco-elasto-plastic equations with the resolution of 1023^2 grid cells and $\Delta t = 0.2 \cdot 10^{-5}$ for 2500 loading increments in time. Panel (a) shows the integrated stress σ_{xx} versus time. Panels (b-d) show the accumulated strain $\log_{10} \varepsilon_{II}$ for three different loading steps as shown in panel (a) by red arrows.

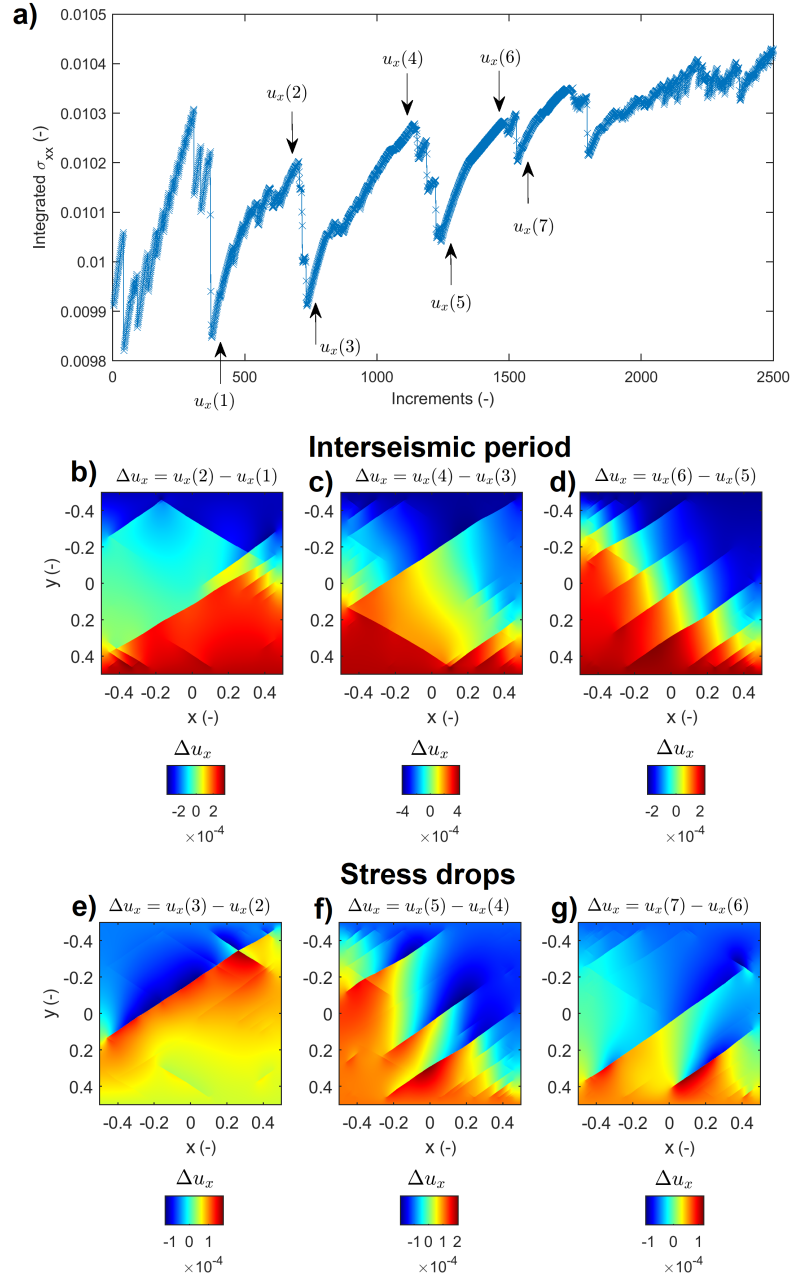
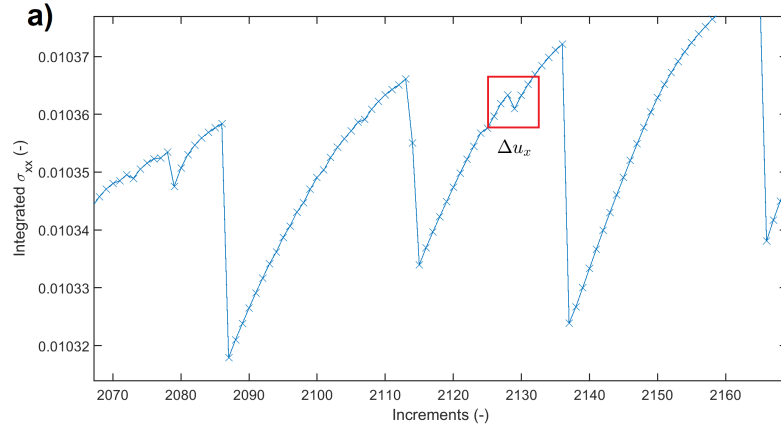
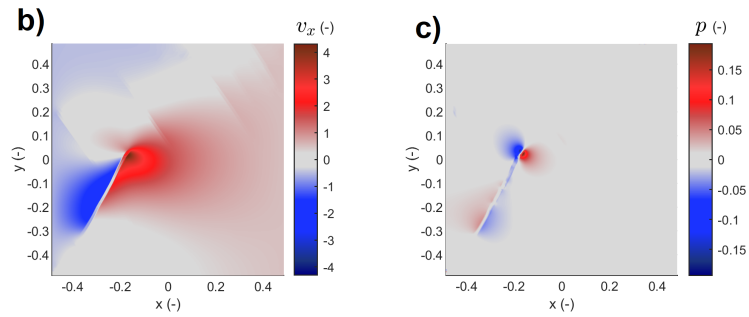


Figure 14: Interseismic period and stress drops: numerical simulation of compressible visco-elasto-plastic equations with the resolution of $N = 1023^2$ grid cells and $\Delta t = 0.2 \cdot 10^{-5}$ for 2500 loading increments in time. Panel (a) shows the integrated stress σ_{xx} versus loading increments. Panels (b-d) show displacement increments Δu_x corresponding to interseismic periods. Panels (e-g) show displacement increments Δu_x corresponding to major stress drops.



Wave field: initial conditions



Wave field after 250 time steps

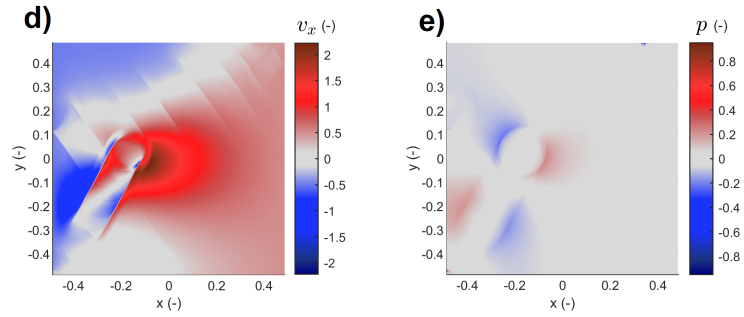


Figure 15: Earthquake nucleation due to a single stress drop. Panel (a) shows the integrated stress σ_{xx} versus loading increments. Panels (b-c) show the wave fields (velocity v_x and pressure p) at the initial stage. Panels (d-e) show wave fields (velocity v_x and pressure p) after 250 time steps.

4.7 Stress drops in three-dimensional simulations

4.7.1 Convergence tests for a single stress drop

Figure 16a shows the integrated stress σ_{xx} versus time of a model with the resolution of $511^3 \approx 133.432.831$ grid cells for a set of different temporal discretizations ($\Delta t = 0.2 \cdot 10^{-5}$, $\Delta t = 0.8 \cdot 10^{-5}$ and $\Delta t = 4.0 \cdot 10^{-5}$). Similarly to the two-dimensional results, the integrated stress σ_{xx} evolution with loading increments is different depending on the temporal discretization. The simulations with finer temporal discretization ($\Delta t = 0.2 \cdot 10^{-5}$, $\Delta t = 0.8 \cdot 10^{-5}$) are similar and lead to sharp drops in σ_{xx} and lower minimum values of stress σ_{xx} . The simulation with coarse temporal discretization ($\Delta t = 4.0 \cdot 10^{-5}$) exhibits completely different evolution of the integrated stress σ_{xx} , which means that the temporal discretization plays an important role in the accuracy of the numerical simulations. Similarly to the two-dimensional results, the minimum of σ_{xx} converges to a constant value as temporal resolution increases. Figure 16b shows the integrated stress σ_{xx} versus time for a set of different spatial discretizations ($\Delta t = 0.8 \cdot 10^{-5}$). The simulations with finer spatial discretizations lead to lower minimum values of stress σ_{xx} . As in two-dimensional examples, a fine spatial and temporal resolutions are needed to accurately describe the stress drop and to evaluate the minimum values of stress σ_{xx} corresponding to stress drops.

4.7.2 Stress drops sequence

Figure 17 shows the results of a numerical simulation with the resolution of $511^3 \approx 133.432.831$ grid cells and $\Delta t = 0.8 \cdot 10^{-5}$ for 250 loading increments in time. In total, four sharp stress drops in the integrated stress σ_{xx} are visible; the stress drops magnitudes are also different. The place and magnitude of the stress drops is spontaneous as in the two-dimensional simulations.

5 Discussion

There are three main numerical parameters which are crucial for the proper numerical simulations of strain localization: a high spatial resolution, a high temporal resolution and the convergence of iterations at each loading increment to the precision of $err = 10^{-12}$. If one of these three conditions is not satisfied — the numerical results might be inaccurate and show a symmetric pattern. According to our tests, a resolution of 500×500 grid cells or more is usually sufficient to resolve the strain localization pattern. To analyze the evolution of the angle of shear bands, a resolution of 1000×1000 or more is needed. However, only small loading increments made it possible to observe sharp stress drops. Sharper stress drops are observed in simulations with smaller loading increments (Figures 5g, 12a, 16a).

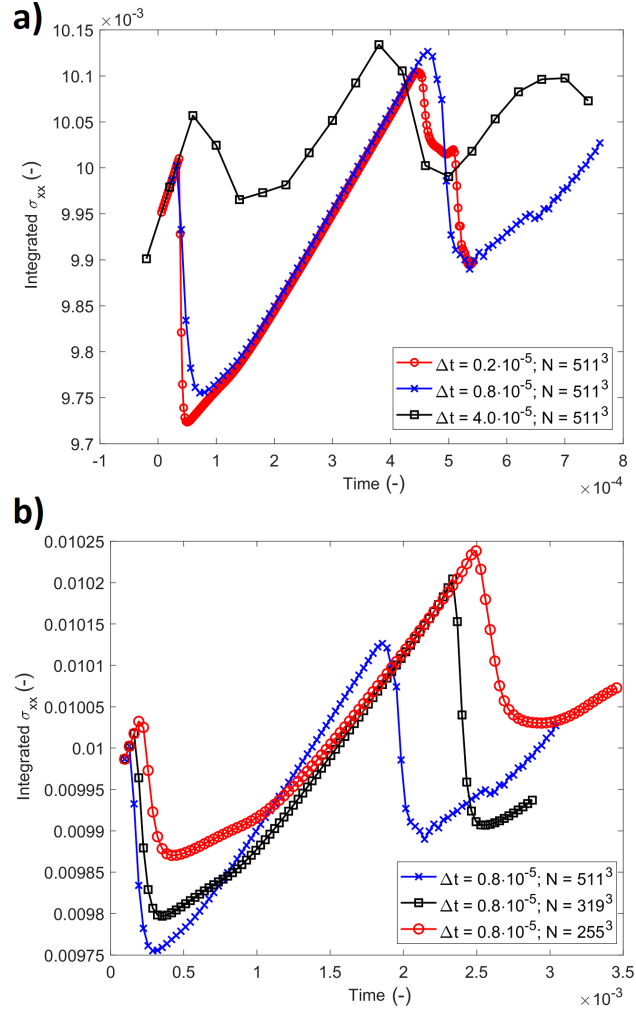


Figure 16: Panel (a) — integrated stress σ_{xx} versus time of a model with the resolution of $511^3 \approx 133.432.831$ grid cells for a set of different temporal discretizations ($\Delta t = 0.2 \cdot 10^{-5}$, $\Delta t = 0.8 \cdot 10^{-5}$ and $\Delta t = 4.0 \cdot 10^{-5}$). Panel (b) — integrated stress σ_{xx} versus time of a model with different spatial discretizations ($\Delta t = 0.8 \cdot 10^{-5}$).

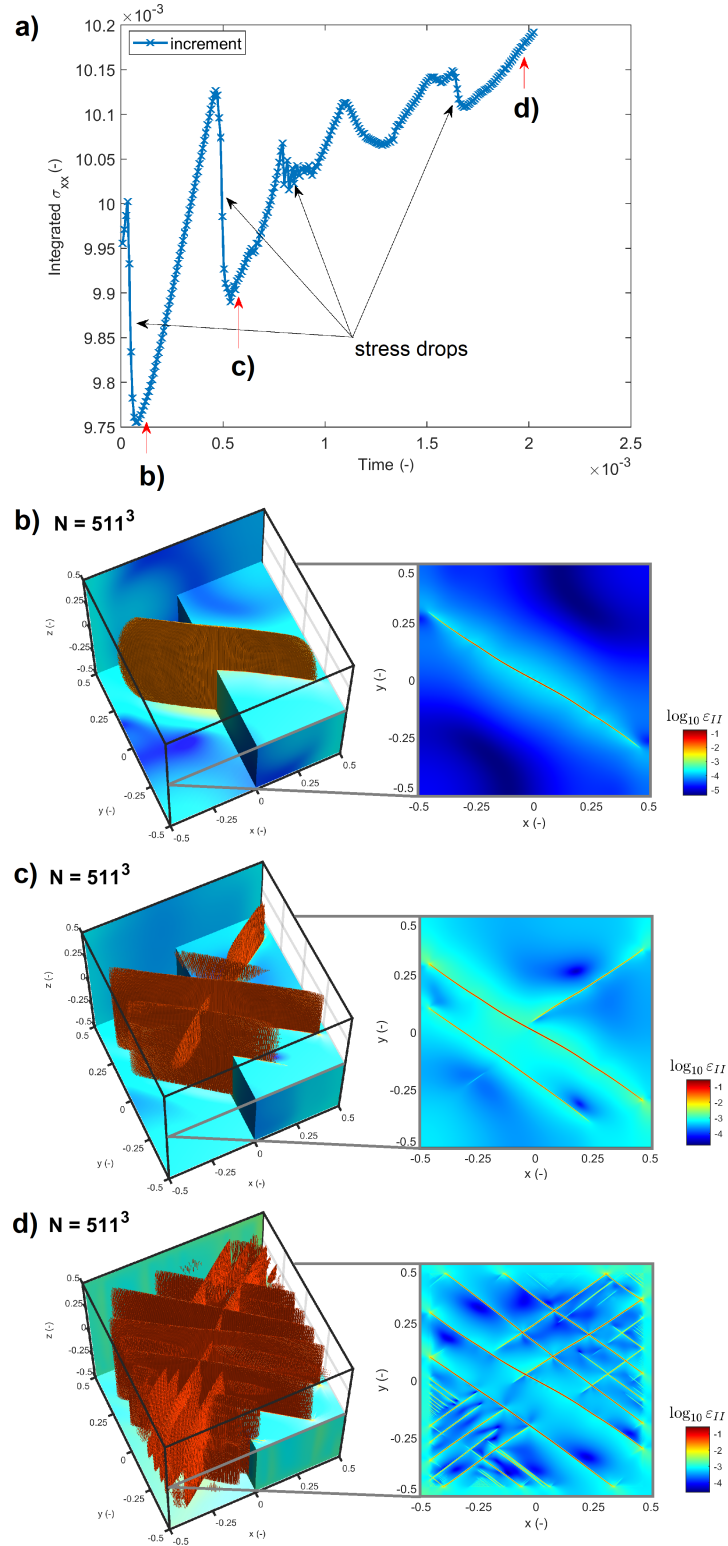


Figure 17: Numerical simulation of compressible visco-elasto-plastic equations with the resolution of 511^3 grid cells and $\Delta t = 0.8 \cdot 10^{-5}$ for 250 increments in time. Panel (a) shows the integrated stress σ_{xx} versus increments in time; panels (b-d) show the accumulated strain $\log_{10} \epsilon_{II}$ for three different times as shown in panel (a).

6 Conclusions

Numerical simulations have been performed addressing different aspects of the modeling of incompressible and compressible visco-elasto-plastic inertialess equations. We have shown that the strain localization pattern as well as velocity discontinuity are equally presented in both elastic and viscous limits of the incompressible visco-elasto-plastic equations. We have presented a high resolution two-dimensional simulation of $\approx 10000^2$ grid cells and showed that the shear band grows under two different angles during its evolution. We concluded that there are three main numerical parameters which are crucial for the proper numerical simulations of strain localization: a high spatial resolution, a high temporal resolution and the convergence of iterations at each loading increment to the precision of $\epsilon_{\text{rel}} = 10^{-12}$. If one of these three conditions is not satisfied — the numerical results might be inaccurate. We have investigated the integrated stress of the model at each loading increment and found that it exhibit sudden stress drops. Such stress drops are spontaneous and exhibit different magnitudes. We have analyzed the spatial and temporal convergence of two- and three- dimensional simulations with the spatial resolution of $\approx 1000^2$ and $\approx 500^3$ grid cells, respectively. Large two- and three-dimensional simulations leading to multiple stress drops are also presented. Such stress drops may correspond to the sequence of earthquakes, therefore, further research is needed.

A The objective stress terms

After expanding, collecting and rearranging terms, the objective stress terms $\tau_{ij}^{\mathcal{R}}$ for a three-dimensional configuration are (in Voigt notation)

$$\sigma_{xx}^{\mathcal{R}} = 2(\sigma_{xy}\dot{\omega}_{xy} + \sigma_{xz}\dot{\omega}_{xz}), \quad (56)$$

$$\sigma_{yy}^{\mathcal{R}} = -2(\sigma_{xy}\dot{\omega}_{xy} - \sigma_{yz}\dot{\omega}_{yz}), \quad (57)$$

$$\sigma_{zz}^{\mathcal{R}} = -2(\sigma_{xz}\dot{\omega}_{xz} + \sigma_{yz}\dot{\omega}_{yz}), \quad (58)$$

$$\sigma_{xy}^{\mathcal{R}} = \dot{\omega}_{xy}(\sigma_{yy} - \sigma_{xx}) + \sigma_{yz}\dot{\omega}_{xz} + \sigma_{xz}\dot{\omega}_{yz}, \quad (59)$$

$$\sigma_{yz}^{\mathcal{R}} = \dot{\omega}_{yz}(\sigma_{zz} - \sigma_{yy}) - \sigma_{xy}\dot{\omega}_{xz} - \sigma_{xz}\dot{\omega}_{xy}, \quad (60)$$

$$\sigma_{xz}^{\mathcal{R}} = \dot{\omega}_{xz}(\sigma_{zz} - \sigma_{xx}) + \sigma_{yz}\dot{\omega}_{xy} - \sigma_{xy}\dot{\omega}_{yz}, \quad (61)$$

and, for a two-dimensional configuration assuming plane strain conditions, Eqs. 56, 57 and 59 reduce to

$$\sigma_{xx}^{\mathcal{R}} = 2\sigma_{xy}\dot{\omega}_{xy}, \quad (62)$$

$$\sigma_{yy}^{\mathcal{R}} = -2\sigma_{xy}\dot{\omega}_{xy}, \quad (63)$$

$$\sigma_{xy}^{\mathcal{R}} = \dot{\omega}_{xy}(\sigma_{yy} - \sigma_{xx}). \quad (64)$$

Acknowledgements

Yury Alkhimenkov gratefully acknowledges support from the Swiss National Science Foundation, project number P500PN_206722. Authors gratefully acknowledge support from the Ministry of Education and Science of Russian Federation (grant №075-15-2022-1106).

Author contributions

YA: Conceptualization, Methodology, Software, Writing – Original Draft, Visualization, Investigation, Formal analysis, Project administration. **LK:** Methodology, Software, Writing – review & editing. **IU:** Methodology, Software, Writing – review & editing. **YP:** Conceptualization, Methodology, Software, Writing – review & editing, Supervision.

Data Availability Statement

No data were used in producing this manuscript.

References

- Aagaard, B. T., Knepley, M. G., and Williams, C. A. (2013). A domain decomposition approach to implementing fault slip in finite-element models of quasi-static and dynamic crustal deformation. *Journal of Geophysical Research: Solid Earth*, 118(6):3059–3079.
- Alkhimenkov, Y., Khakimova, L., and Podladchikov, Y. (2021a). Stability of discrete schemes of biot’s poroelastic equations. *Geophysical Journal International*, 225(1):354–377.
- Alkhimenkov, Y., Räss, L., Khakimova, L., Quintal, B., and Podladchikov, Y. (2021b). Resolving wave propagation in anisotropic poroelastic media using graphical processing units (gpu). *Journal of Geophysical Research: Solid Earth*, 126(7):e2020JB021175.
- Allison, K. L. and Dunham, E. M. (2018). Earthquake cycle simulations with rate-and-state friction and power-law viscoelasticity. *Tectonophysics*, 733:232–256.
- Balay, S., Abhyankar, S., Adams, M., Brown, J., Brune, P., Buschelman, K., Dalcin, L., Dener, A., Eijkhout, V., Gropp, W., et al. (2019). *Petsc users manual*.
- Baumgardner, J. R. (1985). Three-dimensional treatment of convective flow in the earth’s mantle. *Journal of Statistical Physics*, 39:501–511.
- Braun, J., Thieulot, C., Fullsack, P., DeKool, M., Beaumont, C., and Huisman, R. (2008). Douar: A new three-dimensional creeping flow numerical model for the solution of geological problems. *Physics of the Earth and Planetary Interiors*, 171(1-4):76–91.
- Buck, W. R. (1993). Effect of lithospheric thickness on the formation of high-and low-angle normal faults. *Geology*, 21(10):933–936.
- Burstedde, C., Ghattas, O., Gurnis, M., Stadler, G., Tan, E., Tu, T., Wilcox, L. C., and Zhong, S. (2008). Scalable adaptive mantle convection simulation on petascale supercomputers. In *SC’08: Proceedings of the 2008 ACM/IEEE Conference on Supercomputing*, pages 1–15. IEEE.
- Cundall, P. (1989). Numerical experiments on localization in frictional materials. *Ingenieur-archiv*, 59:148–159.
- Cundall, P. (1990). Numerical modelling of jointed and faulted rock. In *International conference on mechanics of jointed and faulted rock*, pages 11–18.

- Dabrowski, M., Krotkiewski, M., and Schmid, D. (2008). Milamin: Matlab-based finite element method solver for large problems. *Geochemistry, Geophysics, Geosystems*, 9(4).
- Dal Zilio, L., Lapusta, N., Avouac, J.-P., and Gerya, T. (2022). Subduction earthquake sequences in a non-linear visco-elasto-plastic megathrust. *Geophysical Journal International*, 229(2):1098–1121.
- Davies, D. R., Davies, J. H., Bollada, P. C., Hassan, O., Morgan, K., and Nithiarasu, P. (2013). A hierarchical mesh refinement technique for global 3-d spherical mantle convection modelling. *Geoscientific Model Development*, 6(4):1095–1107.
- Davies, D. R., Wilson, C. R., and Kramer, S. C. (2011). Fluidity: A fully unstructured anisotropic adaptive mesh computational modeling framework for geodynamics. *Geochemistry, Geophysics, Geosystems*, 12(6).
- De Borst, R., Crisfield, M. A., Remmers, J. J., and Verhoosel, C. V. (2012). *Nonlinear finite element analysis of solids and structures*. John Wiley & Sons.
- de Borst, R. and Duretz, T. (2020). On viscoplastic regularisation of strain-softening rocks and soils. *International Journal for Numerical and Analytical Methods in Geomechanics*, 44(6):890–903.
- de Souza Neto, E. A., Peric, D., and Owen, D. R. (2011). *Computational methods for plasticity: theory and applications*. John Wiley & Sons.
- Deng, J., Gurnis, M., Kanamori, H., and Hauksson, E. (1998). Viscoelastic flow in the lower crust after the 1992 landers, california, earthquake. *Science*, 282(5394):1689–1692.
- Dieterich, J. H. (1978). Time-dependent friction and the mechanics of stick-slip. *Rock friction and earthquake prediction*, pages 790–806.
- Dieterich, J. H. (1979). Modeling of rock friction: 1. experimental results and constitutive equations. *Journal of Geophysical Research: Solid Earth*, 84(B5):2161–2168.
- Dormy, E. and Tarantola, A. (1995). Numerical simulation of elastic wave propagation using a finite volume method. *Journal of Geophysical Research: Solid Earth*, 100(B2):2123–2133.
- Drucker, D. C. and Prager, W. (1952). Soil mechanics and plastic analysis or limit design. *Quarterly of applied mathematics*, 10(2):157–165.
- Duretz, T., de Borst, R., and Le Pourhiet, L. (2019a). Finite thickness of shear bands in frictional viscoplasticity and implications for lithosphere dynamics. *Geochemistry, Geophysics, Geosystems*, 20(11):5598–5616.

- Duretz, T., de Borst, R., and Yamato, P. (2021). Modeling lithospheric deformation using a compressible visco-elasto-viscoplastic rheology and the effective viscosity approach. *Geochemistry, Geophysics, Geosystems*, 22(8):e2021GC009675.
- Duretz, T., de Borst, R., Yamato, P., and Le Pourhiet, L. (2020). Toward robust and predictive geodynamic modeling: The way forward in frictional plasticity. *Geophysical Research Letters*, 47(5):e2019GL086027.
- Duretz, T., Räss, L., Podladchikov, Y., and Schmalholz, S. (2019b). Resolving thermomechanical coupling in two and three dimensions: spontaneous strain localization owing to shear heating. *Geophysical Journal International*, 216(1):365–379.
- Farrington, R., Moresi, L.-N., and Capitanio, F. A. (2014). The role of viscoelasticity in subducting plates. *Geochemistry, Geophysics, Geosystems*, 15(11):4291–4304.
- Forsyth, D. W. (1992). Finite extension and low-angle normal faulting. *Geology*, 20(1):27–30.
- Frankel, S. P. (1950). Convergence rates of iterative treatments of partial differential equations. *Mathematics of Computation*, 4(30):65–75.
- Gabriel, A.-A., Ampuero, J.-P., Dalguer, L., and Mai, P. M. (2013). Source properties of dynamic rupture pulses with off-fault plasticity. *Journal of Geophysical Research: Solid Earth*, 118(8):4117–4126.
- Gerya, T. V. and Yuen, D. A. (2007). Robust characteristics method for modelling multiphase visco-elasto-plastic thermo-mechanical problems. *Physics of the Earth and Planetary Interiors*, 163(1-4):83–105.
- Glerum, A., Thieulot, C., Fraters, M., Blom, C., and Spakman, W. (2018). Nonlinear viscoplasticity in aspect: benchmarking and applications to subduction. *Solid Earth*, 9(2):267–294.
- Happel, J. and Brenner, H. (1983). *Low Reynolds number hydrodynamics: with special applications to particulate media*, volume 1. Springer Science & Business Media.
- Hill, R. (1950). *The mathematical theory of plasticity*. Clarendon Press, Oxford.
- Hill, R. (1958). A general theory of uniqueness and stability in elastic-plastic solids. *Journal of the Mechanics and Physics of Solids*, 6(3):236–249.
- Jaquet, Y., Duretz, T., and Schmalholz, S. M. (2016). Dramatic effect of elasticity on thermal softening and strain localization during lithospheric shortening. *Geophysical Journal International*, 204(2):780–784.
- Kachanov, L. M. (1974). *Fundamentals of the Theory of Plasticity*. MIR Publishers, Moscow.
- Kaneko, Y. and Fialko, Y. (2011). Shallow slip deficit due to large strike-slip earthquakes in dynamic rup-

- ture simulations with elasto-plastic off-fault response. *Geophysical Journal International*, 186(3):1389–1403.
- Kaus, B. J. (2010). Factors that control the angle of shear bands in geodynamic numerical models of brittle deformation. *Tectonophysics*, 484(1-4):36–47.
- Kaus, B. J. and Podladchikov, Y. Y. (2006). Initiation of localized shear zones in viscoelastoplastic rocks. *Journal of Geophysical Research: Solid Earth*, 111(B4).
- Kronbichler, M., Heister, T., and Bangerth, W. (2012). High accuracy mantle convection simulation through modern numerical methods. *Geophysical Journal International*, 191(1):12–29.
- Lavier, L. L., Roger Buck, W., and Poliakov, A. N. (1999). Self-consistent rolling-hinge model for the evolution of large-offset low-angle normal faults. *Geology*, 27(12):1127–1130.
- Lemiale, V., Mühlhaus, H.-B., Moresi, L., and Stafford, J. (2008). Shear banding analysis of plastic models formulated for incompressible viscous flows. *Physics of the Earth and Planetary Interiors*, 171(1-4):177–186.
- LeVeque, R. J. (1992). *Numerical methods for conservation laws*, volume 132. Springer.
- May, D. A., Brown, J., and Le Pourhiet, L. (2015). A scalable, matrix-free multigrid preconditioner for finite element discretizations of heterogeneous stokes flow. *Computer methods in applied mechanics and engineering*, 290:496–523.
- May, D. A. and Moresi, L. (2008). Preconditioned iterative methods for stokes flow problems arising in computational geodynamics. *Physics of the Earth and Planetary Interiors*, 171(1-4):33–47.
- Minakov, A. and Yarushina, V. (2021). Elastoplastic source model for microseismicity and acoustic emission. *Geophysical Journal International*, 227(1):33–53.
- Moczo, P., Robertsson, J. O., and Eisner, L. (2007). The finite-difference time-domain method for modeling of seismic wave propagation. *Advances in geophysics*, 48:421–516.
- Moresi, L., Mühlhaus, H.-B., Lemiale, V., and May, D. (2007a). Incompressible viscous formulations for deformation and yielding of the lithosphere. *Geological Society, London, Special Publications*, 282(1):457–472.
- Moresi, L., Quenette, S., Lemiale, V., Meriaux, C., Appelbe, B., and Mühlhaus, H.-B. (2007b). Computational approaches to studying non-linear dynamics of the crust and mantle. *Physics of the Earth and Planetary Interiors*, 163(1-4):69–82.

- Moresi, L., Zhong, S., and Gurnis, M. (1996). The accuracy of finite element solutions of stokes's flow with strongly varying viscosity. *Physics of the Earth and Planetary Interiors*, 97(1-4):83–94.
- Olive, J.-A., Behn, M. D., Mittelstaedt, E., Ito, G., and Klein, B. Z. (2016). The role of elasticity in simulating long-term tectonic extension. *Geophysical Journal International*, 205(2):728–743.
- Omlin, S., Malvoisin, B., and Podladchikov, Y. Y. (2017). Pore fluid extraction by reactive solitary waves in 3-d. *Geophysical Research Letters*, 44(18):9267–9275.
- Omlin, S., Räss, L., and Podladchikov, Y. Y. (2018). Simulation of three-dimensional viscoelastic deformation coupled to porous fluid flow. *Tectonophysics*, 746:695–701.
- Poliakov, A. and Herrmann, H. (1994). Self-organized criticality of plastic shear bands in rocks. *Geophysical Research Letters*, 21(19):2143–2146.
- Poliakov, A., Podladchikov, Y., and Talbot, C. (1993). Initiation of salt diapirs with frictional overburdens: numerical experiments. *Tectonophysics*, 228(3-4):199–210.
- Poliakov, A. N., Herrmann, H. J., Podladchikov, Y. Y., and Roux, S. (1994). Fractal plastic shear bands. *Fractals*, 2(04):567–581.
- Popov, A. and Sobolev, S. V. (2008). Slim3d: A tool for three-dimensional thermomechanical modeling of lithospheric deformation with elasto-visco-plastic rheology. *Physics of the earth and planetary interiors*, 171(1-4):55–75.
- Pranger, C., Sanan, P., May, D. A., Le Pourhiet, L., and Gabriel, A.-A. (2022). Rate and state friction as a spatially regularized transient viscous flow law. *Journal of Geophysical Research: Solid Earth*, 127(6):e2021JB023511.
- Räss, L., Duretz, T., and Podladchikov, Y. (2019). Resolving hydromechanical coupling in two and three dimensions: spontaneous channelling of porous fluids owing to decompaction weakening. *Geophysical Journal International*, 218(3):1591–1616.
- Räss, L., Licul, A., Herman, F., Podladchikov, Y. Y., and Suckale, J. (2020). Modelling thermomechanical ice deformation using an implicit pseudo-transient method (fastice v1. 0) based on graphical processing units (gpus). *Geoscientific Model Development*, 13(3):955–976.
- Räss, L., Utkin, I., Duretz, T., Omlin, S., and Podladchikov, Y. Y. (2022). Assessing the robustness and scalability of the accelerated pseudo-transient method. *Geoscientific Model Development*, 15(14):5757–5786.

- Rice, J. R. and Rudnicki, J. (1980). A note on some features of the theory of localization of deformation. *International Journal of solids and structures*, 16(7):597–605.
- Rudnicki, J. W. and Rice, J. (1975). Conditions for the localization of deformation in pressure-sensitive dilatant materials. *Journal of the Mechanics and Physics of Solids*, 23(6):371–394.
- Ruina, A. (1983). Slip instability and state variable friction laws. *Journal of Geophysical Research: Solid Earth*, 88(B12):10359–10370.
- Scholz, C. H. (2019). *The mechanics of earthquakes and faulting*. Cambridge university press.
- Spiegelman, M., May, D. A., and Wilson, C. R. (2016). On the solvability of incompressible stokes with viscoplastic rheologies in geodynamics. *Geochemistry, Geophysics, Geosystems*, 17(6):2213–2238.
- Sulem, J. and Vardoulakis, I. (1995). *Bifurcation analysis in geomechanics*. CRC Press.
- Tackley, P. J. (1996). Effects of strongly variable viscosity on three-dimensional compressible convection in planetary mantles. *Journal of Geophysical Research: Solid Earth*, 101(B2):3311–3332.
- Tackley, P. J. (2008). Modelling compressible mantle convection with large viscosity contrasts in a three-dimensional spherical shell using the yin-yang grid. *Physics of the Earth and Planetary Interiors*, 171(1-4):7–18.
- Templeton, E. L. and Rice, J. R. (2008). Off-fault plasticity and earthquake rupture dynamics: 1. dry materials or neglect of fluid pressure changes. *Journal of Geophysical Research: Solid Earth*, 113(B9).
- Thieulot, C. (2011). Fantom: Two-and three-dimensional numerical modelling of creeping flows for the solution of geological problems. *Physics of the Earth and Planetary Interiors*, 188(1-2):47–68.
- Tong, X. and Lavier, L. L. (2018). Simulation of slip transients and earthquakes in finite thickness shear zones with a plastic formulation. *Nature communications*, 9(1):3893.
- Turcotte, D. L. and Schubert, G. (2002). *Geodynamics*. Cambridge university press.
- Uphoff, C., May, D. A., and Gabriel, A.-A. (2023). A discontinuous galerkin method for sequences of earthquakes and aseismic slip on multiple faults using unstructured curvilinear grids. *Geophysical Journal International*, 233(1):586–626.
- Vardoulakis, I., Goldscheider, M., and Gudehus, G. (1978). Formation of shear bands in sand bodies as a bifurcation problem. *International Journal for numerical and analytical methods in Geomechanics*, 2(2):99–128.

- Vermeer, P. (1990). The orientation of shear bands in biaxial tests. *Géotechnique*, 40(2):223–236.
- Vermeer, P. A. and De Borst, R. (1984). Non-associated plasticity for soils, concrete and rock. *HERON*, 29 (3), 1984.
- Virieux, J. (1986). P-sv wave propagation in heterogeneous media: Velocity-stress finite-difference method. *Geophysics*, 51(4):889–901.
- Virieux, J. and Madariaga, R. (1982). Dynamic faulting studied by a finite difference method. *Bulletin of the Seismological Society of America*, 72(2):345–369.
- Wilson, C. R., Spiegelman, M., and van Keken, P. E. (2017). Terra ferma: The transparent finite element rapid model assembler for multiphysics problems in earth sciences. *Geochemistry, Geophysics, Geosystems*, 18(2):769–810.
- Wollherr, S., Gabriel, A.-A., and Uphoff, C. (2018). Off-fault plasticity in three-dimensional dynamic rupture simulations using a modal discontinuous galerkin method on unstructured meshes: implementation, verification and application. *Geophysical Journal International*, 214(3):1556–1584.
- Zienkiewicz, O. C. and Taylor, R. L. (2005). *The finite element method for solid and structural mechanics*. Elsevier.
- Zienkiewicz, O. C., Taylor, R. L., and Nithiarasu, P. (2013). *The finite element method for fluid dynamics*. Butterworth-Heinemann.